

Galaxy properties from J-PAS narrow-band photometry

A. Mejía-Narváez^{1,2*}, G. Bruzual³, G. Magris C.¹, J. S. Alcaniz⁴, N. Benítez⁵,
S. Carneiro⁶, A. J. Cenarro⁷, D. Cristóbal-Hornillos⁷, R. Dupke^{4,8}, A. Ederoclite⁷,
A. Marín-Franch⁷, C. Mendes de Oliveira⁹, M. Moles⁷, L. Sodre Jr.⁹, K. Taylor^{4,9},
J. Varela⁷, and H. Vázquez Ramió⁷

¹Centro de Investigaciones de Astronomía, AP 264, Mérida 5101-A, Venezuela.

²Posgrado en Física Fundamental, Universidad de Los Andes, Mérida, Venezuela.

³Instituto de Radioastronomía y Astrofísica, IRyA, UNAM, Campus Morelia, A.P. 3-72, C.P. 58089, Morelia, Michoacán, México.

⁴Observatório Nacional-MCT, Rua José Cristino, 77. CEP 20921-400 Rio de Janeiro-RJ, Brazil.

⁵Instituto de Astrofísica de Andalucía (IAA-CSIC), Glorieta de la Astronomía s/n, E-18008 Granada, Spain.

⁶Instituto de Física, Universidade Federal da Bahia, 40210-340 Salvador, Bahia, Brazil.

⁷Centro de Estudios de Física del Cosmos de Aragón, Plaza San Juan 1, E-44001 Teruel, Spain.

⁸Department of Astronomy, University of Michigan, Ann Arbor, MI 48109, USA.

⁹Instituto de Astronomia, Geofísica e Ciências Atmosféricas, Universidade de São Paulo, Cidade Universitária, 05508-090 São Paulo, Brazil.

18 November 2021

ABSTRACT

We study the consistency of the physical properties of galaxies retrieved from SED-fitting as a function of spectral resolution and signal-to-noise ratio (SNR). Using a selection of physically motivated star formation histories, we set up a control sample of mock galaxy spectra representing observations of the local Universe in high-resolution spectroscopy, and in 56 narrow-band and 5 broad-band photometry. We fit the SEDs at these spectral resolutions and compute their corresponding the stellar mass, the mass- and luminosity-weighted age and metallicity, and the dust extinction. We study the biases, correlations, and degeneracies affecting the retrieved parameters and explore the rôle of the spectral resolution and the SNR in regulating these degeneracies. We find that narrow-band photometry and spectroscopy yield similar trends in the physical properties derived, the former being considerably more precise. Using a galaxy sample from the SDSS, we compare more realistically the results obtained from high-resolution and narrow-band SEDs (synthesized from the same SDSS spectra) following the same spectral fitting procedures. We use results from the literature as a benchmark to our spectroscopic estimates and show that the prior PDFs, commonly adopted in parametric methods, may introduce biases not accounted for in a Bayesian framework. We conclude that narrow-band photometry yields the same trend in the age-metallicity relation in the literature, provided it is affected by the same biases as spectroscopy; albeit the precision achieved with the latter is generally twice as large as with the narrow-band, at SNR values typical of the different kinds of data.

Key words: galaxies: formation – galaxies: evolution – galaxies: stellar content

1 INTRODUCTION

Galaxies are one of the most fundamental building blocks of the visible Universe. Understanding the processes of their formation and evolution is fundamental to constrain theories aimed to explain the development of the large-scale structure observed today. To-

wards this goal we rely on the *light* arriving from distant galaxies, gathered either through photometric or spectroscopic detectors. Spectroscopic observations provide detailed information on a galaxy spectral energy distribution (SED), but due to their high telescope cost, the bulk of the observations collected until now are

* E-mail: mejia@cida.gob.ve

photometric.¹ In the last decade a number of photometric sky surveys have been completed. The Sloan Digital Sky Survey (SDSS; York et al. 2000) in the optical wavelength range, the panchromatic Great Observatories Origins Deep Survey (GOODS; Giavalisco et al. 2004), and the Cosmic Assembly Near-infrared Deep Extragalactic Legacy Survey (CANDELS; Koekemoer et al. 2011) provide imaging data from the UV to the NIR. The availability of these surveys triggered the development of techniques to extract reliable information on the physical properties of galaxies from their SEDs.

It has long been known that the SED encodes information on a galaxy stellar content (Morgan 1956; Wood 1966; Faber 1972; Tinsley 1972). Since the pioneering work of Morgan (1956) on inverse spectral synthesis (IS hereafter), and Tinsley (1972) on stellar population synthesis (SPS), many authors have explored this subject and developed powerful techniques to decode the star formation history (SFH) of unresolved galaxies from their SEDs. SPS (Bruzual & Charlot 2003; Maraston 2005; Conroy & Gunn 2010) provides the simple stellar population (SSP) models feeding both models of galaxy formation and evolution (e. g., De Lucia & Blaizot 2007; Chen et al. 2012; Vogelsberger et al. 2014), and IS codes (e. g., Cid Fernandes et al. 2005). SED fitting has thus become a standard procedure to extract physical information *directly* from galaxy observations, while the adequacy of the SSP models to reproduce such observations is tested on each fit.

Despite this success, prevailing uncertainties on key aspects of the theories of star formation, e. g., the universality of the initial mass function, (Bastian et al. 2010; Conroy et al. 2013), and stellar evolution, e. g., the thermally pulsing phase of AGB stars (MacArthur et al. 2010; Kriek et al. 2010; Zibetti et al. 2013), and on the properties of the interstellar medium and their dependence on galaxy type through cosmic time, e. g., the properties of dust present in the ISM (Kobayashi et al. 2013; Kriek & Conroy 2013), propagate through the integrated spectral analysis, as also do possible instrumentation and calibration errors in spectroscopic or photometric galaxy surveys (e. g. Conroy et al. 2010). The net result of these uncertainties is to blur the conclusions drawn from SED-fitting studies alone.

Apart from the availability of large data samples mentioned above, the use of photometric observations is attractive for a number of reasons. In spectroscopic surveys the flux calibration, the sky emission, along with the limitations introduced by the aperture and multiplexing, are common issues which introduce unwanted sources of systematics in the derived stellar content of galaxies (see Walcher et al. 2011; Conroy 2013, for reviews). Photometric surveys, on the other hand, are in principle free from these issues. Furthermore, broad-band optical galaxy colours show little sensitivity to the IMF slope (Hansson et al. 2012) and to complex abundance patterns, such as the enhancement of α elements in early-type galaxies (Greggio 1997; Maraston et al. 2003). SED-fitting of photometric data can then proceed safely assuming a universal IMF and the widely implemented solar abundance pattern. Nonetheless, this advantage is defeated by the lack of ability of most photometric observations to provide any clue on the metal content of galaxies (however, see Bell & de Jong 2000; MacArthur et al. 2010), given the high spectral resolution required to reach an accurate estimate of this parameter (e. g. Pforr et al. 2012). Likewise, estimating photometric redshifts usually demands the implementation of sophisticated methods in order to overcome multiple degeneracies and

achieve results comparable to spectroscopic redshifts (e. g. Benítez 2000; Oyaizu et al. 2008).

The ideal galaxy survey designed to provide reliable estimations of the stellar content of unresolved galaxies would thus combine the strengths of spectroscopy and photometry, namely: spectral resolution and wavelength sampling good enough to allow for accurate determination of physical properties (including metallicity and redshift), and large and deep sky coverage to allow for large volume-limited samples. Photometric surveys with these characteristics and goals already exist, e. g. COMBO-17 (Wolf et al. 2003) and ALHAMBRA (Moles et al. 2008), allowing for the study of the global physical properties of distant galaxies (see e. g. Díaz-García et al. 2015), but still restricted to certain aspects of galaxy formation and evolution because of limited sky coverage and/or coarse wavelength sampling, due to the use of a small number of intermediate width (FWHM $> 200 \text{ \AA}$) passbands.

The Javalambre-PAU Astrophysical Survey (J-PAS Benítez et al. 2014; Dupke et al. 2015) will gather data for $\sim 1/5$ of the sky in 54 narrow-band (FWHM = 145 \AA) and 2 broad-band filters, covering the optical range from ~ 3500 up to 10000 \AA (Marin-Franch et al. 2015). The main goal of the J-PAS collaboration is to measure the baryonic acoustic oscillations (BAOs), for which the instruments are designed to provide photo- z estimates for a large number of galaxies with accuracy $\approx 0.003(1+z)$, comparable to spectroscopic redshifts. Therefore, this survey will be a unique laboratory for galaxy formation and evolution studies. Given the wavelength coverage of J-PAS, it is anticipated that the galaxy mass, age, and metallicity estimates will supersede the limitations imposed by traditional photometry, but the figures of merit still remain to be derived. On the eve of the start of J-PAS, in this paper we study to what extent the properties of galaxies can be derived from its narrow-band photometric data using a non-parametric SED fitting code such as DynBaS, described by Magris et al. (2015, hereafter M15). We select a test sample of $\sim 10^4$ nearby galaxies ($z < 0.1$) from the SDSS-DR7 (York et al. 2000; Abazajian et al. 2009) and synthesize the photometry through the 56 narrow-band response functions. This sample spans a variety of SFHs, allowing us to confront the well-studied age-metallicity relation (AMR) derived from spectroscopic data (see Gallazzi et al. 2005; Sánchez et al. 2012; González Delgado et al. 2014, and references therein), with our photometric derivation of the AMR.

In §2 and §3 we describe the galaxy samples and the SED fitting method, respectively. In §4 we compare the merits of SED-fitting galaxy spectra at the resolution of spectroscopic and narrow-band photometric data sets, using mock data. In §5 we analyse the insights on stellar metallicity obtained from spectroscopic SED fits, and, using this result as a benchmark, we study the corresponding results for the narrow-band fits, both based on observed data. In §6 we present our conclusions.

2 GALAXY SAMPLES

2.1 The observed galaxy sample

We draw a sample of $\sim 7k$ galaxy spectra from the SDSS-DR7 (Abazajian et al. 2009) by requiring that the SEDs have: (i) $z \leq 0.09$ to remain in the optical range; (ii) signal-to-noise ratio > 10 to minimise degeneracies in the physical parameters recovered from the spectral fits; and (iii) a fraction of good pixels $\gtrsim 95$ per cent. A narrow wavelength range ($\approx 20 \text{ \AA}$) centred at the [O II] $\lambda\lambda 3726, 3729, \text{H}\gamma, \text{H}\beta, [\text{O III}] \lambda\lambda 4959, 5007, \text{He I} \lambda 5876,$

¹ Energy distributions measured through a series of conveniently located photometric bands can be regarded as *ultra-low resolution* SEDs.

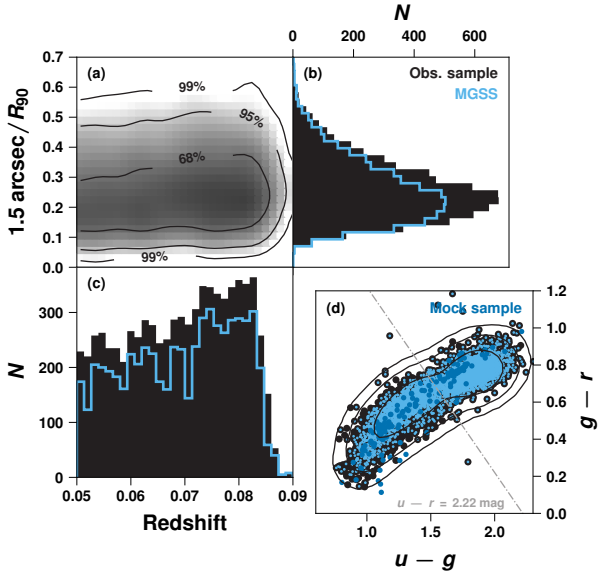


Figure 1. (a) The fraction of light entering the 1.5 arcsec fibre radius with respect to the 90 per cent petrosian radius ($1.5 \text{ arcsec}/R_{90}$) as a function of redshift is shown as evidence of the absence of aperture bias in the observed galaxy sample. The corresponding y-axis (b) and x-axis (c) marginal distributions are shown (black), along with the MPA-Garching subset (MGSS, light blue histograms). (d) $u - g$ vs. $g - r$ colour-colour distribution of the observed galaxy sample described in §2 (black dots and 1σ , 2σ , and 3σ confidence regions as contours), the MGSS (light blue dots), and the mock galaxy sample (dark blue dots). The colour separator $u - r = 2.22 \text{ mag}$ (Strateva et al. 2001) is shown as a dot-dashed line.

[O I] $\lambda 6300$, [N II] $\lambda \lambda 6548, 6583$, H α and [S II] $\lambda \lambda 6717, 6731$ emission lines is masked out regardless of their presence in the target SED. Finally, the sample is divided into star-forming galaxies (SFGs) and passive galaxies (PaGs) according to the colour separator $u - r = 2.22 \text{ mag}$ (Strateva et al. 2001). The black dots in Fig. 1(d) shows the colour-colour distribution of the resulting sample, the contours correspond to the 1σ , 2σ , and 3σ confidence regions. A subset (MGSS hereafter) of galaxies from our sample was studied by Gallazzi et al. (2005, G05 hereafter) and is highlighted in light blue in Fig. 1. The MGSS² is suitable for setting up a benchmark to compare with our spectroscopic estimates of galaxy properties (see §5.2).

To test the consistency between the parameters derived from spectroscopic data and narrow-band photometric data, we synthesize narrow-band observations from SDSS galaxy spectra as seen at $z = 0$ using the J-PAS throughput (Marin-Franch et al. 2015) shown in Fig. 2. The mean flux expected through the k th passband is given by

$$F_k = \int_{\lambda} f_{\lambda} T_k(\lambda) d\lambda \bigg/ \int_{\lambda} T_k(\lambda) d\lambda, \quad (1)$$

where f_{λ} is the rest-frame SDSS galaxy SED, and $T_k(\lambda)$ is the response function of the k th passband. A measurement of the error in F_k is provided by conventional error propagation (Bevington &

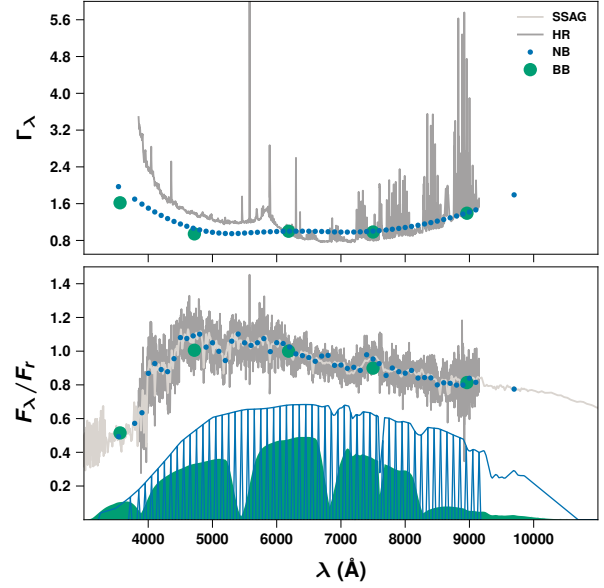


Figure 2. *Top:* Standard deviation spectrum template, Γ_{λ} , for the three spectral resolutions used in this paper. The dark grey line is the mean value of the noise reported for all the galaxies up to $z = 0.1$ in the SDSS DR7, normalised at the effective wavelength of the r' -passband. This curve, smoothed and interpolated at the central wavelength points of the J-PAS passbands response function (blue), is used to calculate the standard deviation for the simulated narrow-band (NB) data. For the broad-band (BB) photometric resolution we use the average of the SDSS imaging reported noise, converted to flux (green). Although a different behaviour in the NB instrumental noise may be expected, the assumed shape reflects the simple fact that the quantum efficiency of most CCD-based optical instruments decrease towards the wavelength extreme values (Howell 2006). *Bottom:* An example SED from the mock sample without noise (light grey) and after adding instrumental noise (dark grey). The NB and the BB versions of the same mock galaxy along with the corresponding passbands throughput (blue and green, respectively) are also shown.

Robinson 2003) using the relation

$$\sigma_k^2 = \int_{\lambda} T_k(\lambda)^2 \sigma_{\lambda}^2 d\lambda, \quad (2)$$

where σ_{λ} is the standard deviation in f_{λ} .

In the ideal case, the SDSS spectra cover the rest-frame wavelength range $3800 - 9200 \text{ \AA}$, whereas the J-PAS filters span $\sim 3500 - 10000 \text{ \AA}$. Hence, around five passbands are naturally masked out. Moreover, those passbands where more than 10 per cent of the pixels are reported as ‘bad’ by the SDSS pipeline are removed from the final narrow-band SEDs. To minimise the impact of missing passbands during SED-fitting, we compute the narrow-band fluxes using the original SDSS spectra, without emission line masking. Then we remove the nebular emission effect *a posteriori*, using a rather simple algorithm to mask out the passband only when an emission line is detected. Overall, the mean number of passbands with potential information on the stellar age and metallicity masked out (including the emission affected passbands) is ~ 15 .

2.2 The mock galaxy sample

To assess the physical properties retrieved from high-resolution spectroscopic, narrow-band and broad-band ($u'g'r'i'z'$, Doi et al.

² available at <http://www.mpa.mpa-garching.mpg.de/SDSS/>.

2010) spectral fits (hereafter HR, NB and BB, respectively), we select a sample of 134 mock galaxies from the Synthetic Spectral Atlas of Galaxies (SSAG hereafter) built by [Cabrera-Ziri & Mejía-Narváez \(2014\)](#), used by [M15](#), and described in Appendix A. We require that the selected galaxies (dark blue dots in Fig. 1(d)) reproduce the observed properties of galaxies, such as the bimodality in the colour $u - r$ and in the 4000 Å-break index distributions ([Stratova et al. 2001](#); [Kauffmann et al. 2003](#); [Baldry et al. 2004](#)). Finally, to emphasise the difference between the mock SEDs at the HR and NB spectral resolutions and their observed counterparts, due to instrumental artefacts and emission line masking, we label the latter as HR* and NB*, respectively.

In order to simulate observed SEDs at the spectral resolution of the NB and BB photometry, and HR spectroscopy, we proceed as follows: (i) from the mock galaxy SED we compute the photometric flux through the passband using Eq. (1).³ (ii) To mimic more realistically galaxy observations, we add Gaussian random noise to the computed fluxes, assuming observationally motivated uncorrelated error sources. For this purpose, we use as a template for generating the standard deviation on F_λ , the averaged error spectra normalized to one at the r' -passband, Γ_λ , for galaxies in the SDSS up to $z = 0.1$, smoothed and degraded in resolution if needed to match each SED type as shown in Fig. 2. Then the actual standard deviation is simply $\Gamma_\lambda F_\lambda / \text{SNR}_r$, given a value for the SNR_r at the effective wavelength of the r' -passband, as in [M15](#).⁴ We note that the flux adds linearly while the noise adds quadratically when synthesizing the flux using the Eq. (1). Therefore, to ensure a fair comparison between the mock sample results and those drawn from the observed sample as a function of the spectral resolution, we assume different values of the signal-to-noise ratio for the different flavours of SEDs: $\text{SNR}_r = 20, 45, \text{ and } 140$ for HR, NB, BB, respectively. To account for statistical variations, the procedure to add noise is repeated 20 times for each SED. The final mock galaxy sample then comprises 2680 SEDs, representative of the local Universe. Once the process of adding observational noise is completed, each mock galaxy SED is passed as input to our spectral fitting code at their HR, NB and BB spectral resolutions, i. e. without any spectral masking. The differences between the HR, NB and the HR*, NB* data sets, respectively, are noteworthy in the context of a potential comparison between the mock and the observed sample results; we will discuss further in §5, where is more appropriate.

Despite the motivation stated above, the chosen SNR_r values deserve further justification in the context of current galaxy surveys. The assumed value of $\text{SNR}_r = 20$ for the mock spectroscopy can be justified straightforwardly if compared to the observed sample described in §2.1 which is characterized by a median $\text{SNR} = 18.8$ across the wavelength range. The value of $\text{SNR}_r = 140$ chosen for the BB photometry, on the other hand, corresponds to a standard deviation of 0.007 mag,⁵ which is comparable to the median error 0.006 mag in r' -passband for the SDSS observed sample. Both of these values are roughly typical of galaxies with $r \sim 18$ mag within an aperture of 3 arcsec. To justify the $\text{SNR}_r = 45$ chosen for the NB mock SEDs, we select three galaxies from the SDSS spectroscopic sample with magnitude $r \sim 19, 18,$

and 17 mag and $\text{SNR} \sim 10, 16, \text{ and } 32$ across all the wavelength range, respectively. For these galaxies we compute the expected SNR at the NB resolution using the formula

$$\text{SNR} = \frac{\bar{F}\bar{T}t}{\sqrt{\bar{F}\bar{T}t + N_{\text{pixel}}N_{\text{read}}\sigma_{\text{read}}^2}}, \quad (3)$$

and the instrumental setting for the J-PAS ([Benitez et al. 2014](#)), where \bar{F} is the mean photon count per second for each source, $\bar{T} = 0.5$ is the mean camera response, $t = t_{\text{exp}}N_{\text{filter}}N_{\text{read}}$ is the total exposure time, $t_{\text{exp}} = 60$ sec is the exposure time per filter per number of readouts, $N_{\text{read}} = 4$ is the number of readouts of the filter array, $N_{\text{filter}} = 56$ is the number of filters, $N_{\text{pixel}} = \pi N_{\text{filter}}(D/2/p_s)^2$ is the total number of pixels within a $D = 3$ arcsec aperture, assuming a pixel scale $p_s = 0.227$ arcsec pixel⁻¹. We consider no sky nor dark current contributions to the total noise (i. e. bright sources only). For the three sources with $r \sim 19, 18, \text{ and } 17$ mag, we find an exposure time per filter per readout, $t_{\text{exp}} \sim 180, 75, 40$ sec. Thus the assumed $\text{SNR}_r = 45$ is observationally plausible only for bright sources in the local Universe according to the planned ($t_{\text{exp}} = 60$ sec) J-PAS configuration. By running the same calculation using the SDSS imaging set up, namely: $\bar{T} = 0.5, t_{\text{exp}} = 60$ sec, $N_{\text{filter}} = 5, D = 3$ arcsec, $p_s = 0.396$ arcsec pixel⁻¹; we find the brightest ($r = 17$ mag) source requires a shorter exposure in order to reach a $\text{SNR}_r = 140$, while the $r = 18$ and 19 mag sources would require > 1 and > 3 scans, respectively. Interestingly, the SDSS spectroscopic set up: $\bar{T} = 0.3, N_{\text{read}} = 5, 3$ and 3 (for the $r \sim 19, 18, \text{ and } 17$ mag sources, respectively), $t_{\text{exp}} = 900$ sec and $N_{\text{pixel}} = 2RD/p_s$, with mean spectral resolution $R = 1800, D = 3$ arcsec and $p_s = 0.396$ arcsec pixel⁻¹, requires a total exposure time for the brightest source about 2 times shorter than J-PAS imaging to reach a $\text{SNR} = 20$. This may suggest that planning a project like J-PAS is a pointless task. However there are at least two key aspects that we have ignored during this exercise. First, photometric surveys do not suffer from aperture effects. Hence, depending on the observing conditions, J-PAS should require a shorter exposure t_{exp} to reach a $\text{SNR} = 20$, characteristic of a spectroscopic survey like SDSS. Second and most important, multi-object imaging is limited mainly by the field of view of the camera, whereas multiplexed spectroscopy usually suffers from engineering limitations. E. g., the J-PAS camera has a field of view of 4.7 square degrees, capable of imaging $\sim 10^4$ galaxies in one exposure, whereas the SDSS-DR7 spectroscopic camera, having a similar field of view, is limited to 640 objects per exposure. See §1 in [Benitez et al. \(2014\)](#) for several other factors favoring photometric surveys over spectroscopic ones.

Overall, the assumed values of the SNR can be reached only for bright sources in the local Universe and our mock sample is thus suitable as a basis of comparison with the observed sample. Given the known impact of data quality on the galaxy physical properties inferred through SED-fitting, in §3.4 we discuss the effects of the SNR_r on the reliability of the stellar content derived for the three spectral resolutions used in this study.

3 GALAXY PROPERTIES FROM SED-FITTING

3.1 On SED-fitting

Spectral fitting algorithms can be classified according to the assumptions made to model the galaxy SFH as parametric and non-parametric. The parametric methods assume a fixed functional form for the SFH and prescribe physically motivated prior distributions

³ In this case we use a version of the SED in which the stellar kinematic effects are not included.

⁴ Different regions of the optical spectra trace different stellar populations. Hence, properly weighting each region during spectral fitting by using an observationally based σ_λ spectrum is crucial to furnish realistic estimates of the uncertainties on the physical properties of the target galaxy.

⁵ Here we use the fact that $\sigma_{\text{magnitude}} \propto 1/\text{SNR}$ ([Howell 2006](#)).

for the intervening parameters (e. g., Kauffmann et al. 2003; Kriek et al. 2009; Hansson et al. 2012), whereas the non-parametric methods (Cid Fernandes et al. 2013; Díaz-García et al. 2015, M15) make no restrictions on the functional shape of the SFH, although some prior assumptions are usually made regarding the time sampling of the SFH in order to minimize potential degeneracies. The parametric approach is generally tackled within the Bayesian framework, where our knowledge about a set of parameters \mathbf{x} posterior to data consideration, $\pi_N(\mathbf{x} | \{\mathcal{D}_i\})$, arises naturally from updating our degree of belief (including prejudices) prior to any data consideration, $\pi_0(\mathbf{x})$, through the likelihood of some assumed model to describe the data, $\mathcal{L}(\{\mathcal{D}_i\} | \mathbf{x})$. According to Bayes' theorem this is

$$\pi_N(\mathbf{x} | \{\mathcal{D}_i\}) \propto \mathcal{L}(\{\mathcal{D}_i\} | \mathbf{x}) \times \pi_0(\mathbf{x}), \quad (4)$$

where $\{\mathcal{D}_i\}$ is the N dimensional data set (e. g., the integrated SED or a number of spectral indices). There are several reasons why this approach is particularly advantageous to the spectral analysis of galaxies. Here we mention two of the most important ones in this context: first, our current knowledge about the data sets and the physics intervening in galaxy formation and evolution allows us to assign in a straightforward manner both the likelihood and the prior distribution; and second, there is no limit (in principle) to the dimensionality of the vector \mathbf{x} , regardless of the size of the data set. This last advantage has been particularly exploited by several authors, who have focused their studies on data sets consisting of a small number ($N \sim 10$) of specific spectral features or photometric data (e. g., Kauffmann et al. 2003; Brinchmann et al. 2004; Tremonti et al. 2004; Gallazzi et al. 2005; Maraston et al. 2010).

In the non-parametric problem, on the other hand, the observed integrated SED F_λ^{obs} of the target galaxy is modelled by maximizing the likelihood. In general it is plausible to assume that the uncertainties on the data are Gaussian and uncorrelated, and that they are described by the proposed model $F_\lambda^{\text{mod}}(\mathbf{x})$, so that the likelihood is given by,

$$\mathcal{L}(F_\lambda^{\text{obs}} | \mathbf{x}) = \prod_{\lambda} \frac{1}{\sqrt{2\pi\sigma_\lambda^2}} \exp\left\{-\frac{[F_\lambda^{\text{obs}} - F_\lambda^{\text{mod}}(\mathbf{x})]^2}{2\sigma_\lambda^2}\right\}, \quad (5)$$

where σ_λ is the standard deviation on F_λ^{obs} . The problem of finding $\hat{\mathbf{x}}$ such that the function above reaches its maximum, is equivalent to minimizing the merit function,

$$-2 \log \mathcal{L} + \text{const} \equiv \chi^2(\mathbf{x}) = \sum_{\lambda} \frac{[F_\lambda^{\text{obs}} - F_\lambda^{\text{mod}}(\mathbf{x})]^2}{\sigma_\lambda^2}. \quad (6)$$

Furthermore, if the proposed model takes the form

$$F_\lambda^{\text{mod}}(\mathbf{x}) = \sum_{k=1}^{N_{\text{SSPs}}} w^k(\mathbf{x}) F_\lambda^k(\mathbf{x}), \quad (7)$$

and the weights $w^k(\mathbf{x})$ are linear on \mathbf{x} , then χ^2 is a quadratic function on the parameter vector \mathbf{x} , and the problem reduces to solving a linear system of N_λ equations with N_{SSPs} unknowns (Cid Fernandes et al. 2005; Ocvirk et al. 2006; Tojeiro et al. 2007).

The main advantage of the non-parametric approach as posed above comes from the simplicity of linearity. This approach has been widely used when the data sets are large enough ($N_\lambda \geq N_{\text{SSPs}}$), so that the system is (over)determined (e. g. GASPEX, TGASPEX in M15). However even in the overdetermined regime, the linear problem is ill-conditioned and the solution $\hat{\mathbf{x}}$ heavily depends on the observed data noise and on model ingredient uncertainties (see discussion in Ocvirk et al. 2006). Furthermore, it does

not provide a straightforward calculation of the uncertainties affecting the best estimate $\hat{\mathbf{x}}$ (however, see Díaz-García et al. 2015, for inspiration), nor does it allow for the inclusion of parameters which, even if physically irrelevant, are needed to fully describe the data set.⁶ On the other hand, current Bayesian studies in the SED-fitting literature lack a thorough assessment of two relevant aspects that may bias galaxy SED interpretations. First, despite the fact that a parametrization of the SFH is not required in the Bayesian framework (see e. g., Da Cunha et al. 2008; Pacifici et al. 2012; Chevallard & Charlot 2016), most authors have opted to assume that star formation is continuous in time after its initial onset, and that the SFH can be described by an exponentially declining (τ -model, Wuyts et al. 2009; Lee et al. 2009), exponentially increasing (inverted τ -model, Maraston et al. 2010), or a 'delayed exponential' (e. g., Hansson et al. 2012) function of time. Second and most important, if a non-objective prior $\pi_0(\mathbf{x})$ is adopted, it needs to be carefully chosen when the data set is not very informative about the parameters through the likelihood (e. g. small and/or low-SNR data set), a regime where it is known that the prior may play an important rôle in shaping the posterior probability distribution (see Benítez 2000; Gallazzi et al. 2008; Chevallard & Charlot 2016, also our discussion in §5.3.3). Both methodologies, Bayesian and maximum likelihood, must agree in their solutions in the limiting case when the adopted likelihood is able to fully span the space of the data set, i. e., when the contribution of the prior distribution becomes irrelevant. The reader is referred to Walcher et al. (2011) for a more thorough discussion on SED fitting approaches.

When introducing a new algorithm, most authors apply their SED fitting procedure to synthetic galaxy spectra of known SFH to compare the true and derived values of parameters like the galaxy stellar mass, mean stellar age, stellar metallicity, and SFR. We will call this procedure theoretical-theoretical assessment (TTA). M15 showed from their TTA that different non-parametric codes using the same SSP ingredients yield, in general, different estimates of the stellar populations present in a galaxy (regardless of the goodness-of-fit), introducing uncertainties in the interpretation of the target galaxy SED. Wuyts et al. (2009); Lee et al. (2009, 2010); Pforr et al. (2012, 2013); Mitchell et al. (2013) have studied the propagation of these uncertainties into the stellar properties derived from photometric energy distributions using parametric SED fitting methods. Pforr et al. (2012); Mitchell et al. (2013); Hayward & Smith (2015) have shown that the τ -models are prone to introducing biases in the retrieved stellar properties when the assumed functional shape of the SFH is in high disagreement with the target SFH (e. g., bursty galaxies). Pforr et al. (2012) show that even using inverted τ -models, the stellar mass, age, and reddening by dust in nearby ($z = 0.5$) galaxies with complex SFHs, cannot be retrieved in a robust manner. Moreover, the correct application of parametric methods to derive physical properties out of incomplete optical spectra (whether photometric or isolated spectroscopic features), usually requires high-quality data and/or independent determinations of some of the physical properties, which are not always available (see e. g., G05; Kriek et al. 2010; Castellano et al. 2014). In this paper we use the non-parametric DynBaS fitting code (§3.2) as an alternative to overcome the limitations of assuming a parametrization for modelling the SED of galaxies from photometric data sets (see also Díaz-García et al. 2015).

⁶ In the Bayesian framework these are the so-called nuisance parameters.

3.2 The DynBaS non-parametric spectral fitting code

Dynamical Basis Selection (DynBaS, M15) is a non-parametric SED fitting code designed to recover the stellar population content of galaxies. The target SED is reconstructed using the model in Eq. 7 with,

$$w^k(\mathbf{x}) = a_{ij}^k, \quad (8a)$$

$$F_\lambda^k(\mathbf{x}) = F_\lambda^k(t_i, Z_j), \quad (8b)$$

where $i = 1, \dots, N_{\text{ages}}$, and $j = 1, \dots, N_{\text{metallicities}}$. The DynBaS code keeps at a minimum the number of spectral components, by combining up to three SSPs ($N_{\text{SSPs}} = 1, 2, \text{ or } 3$), *dynamically selected* for each target galaxy, to yield the absolute minimum of the merit function, χ^2 , in the region of parameter space sampled in the fit. The summation in Eq. (6) runs over the (not masked) N_λ wavelength points in the target SED F_λ^{obs} . Whether the optimal solution F_λ^{mod} is assembled combining 1, 2 or 3 SSPs, depends on the peculiarities of the target SED.

It is worth noting that the DynBaS code is not intended to retrieve the full time resolution SFH of galaxies, but rather to deliver robust estimates of their global physical properties, averaged over their stellar content. The current implementation of DynBaS is suitable for the analysis of stellar populations coarsely sampled spectroscopically and/or with low SNR, formed through complex (cf. §5.2) or simple SFHs (e.g., Cabrera-Ziri et al. 2016). Using SNR = 20 mock spectroscopy, M15 showed that DynBaS recovers such global properties with a bias and precision equivalent to those obtained with methods aimed at SFH recovery (e.g. STARLIGHT, TGASPEX); a result suggesting that in fact galaxies resulting from complex SFHs can be described by the combination of young, intermediate, and old stellar populations (Cid Fernandes et al. 2005).

Indeed several authors have implemented non-parametric models like Eq. (7) with $N_{\text{SSPs}} \sim 5$. For instance, Ocvirk et al. (2006) implemented the STECMAP code which sets N_{SSPs} during the fitting by regulating the prior PDF contribution to the posterior PDF depending on the SNR of the data set. Tojeiro et al. (2007) implemented VESPA, a SED-fitting code that adjusts the number of parameters retrieved from the fit depending on the SNR of the data. Tojeiro et al. found that a spectroscopic sample of SDSS galaxies with SNR > 10 is well represented by the combination of $N_{\text{SSPs}} \sim 5$. Both codes show a dependency of the number of parameters retrieved on the wavelength range, where the inclusion of additional spectral information allows for a higher parameter space resolution. The general trend behind the results drawn from STECMAP, VESPA, and DynBaS is that the amount of physical information retrieved in a robust manner is a function of the size of the data set and its quality, described by some property Q . In fact the number of free parameters on the retrieved SFH should obey a function of the form $N_{\text{SSPs}} = N_{\text{SSPs}}(N_\lambda, Q)$. The authors above have successfully implemented models with $N_{\text{SSPs}}(Q)$, with $Q \equiv \text{SNR}$. The complete function $N_{\text{SSPs}}(N_\lambda, Q)$ remains understudied in the spectral fitting literature regarding non-parametric and parametric methods. In an upcoming paper we will address the dependency of N_{SSPs} on both the data set quality and the wavelength sampling in the context of current multi-band photometric surveys of galaxies.

3.3 Deriving physical parameters

To build F_λ^{mod} in Eqs. (7) and (8) we adopt the same BC03xm SSP models as in the mock sample (Appendix A). If F_λ^{obs} represents

spectroscopic data, F_λ^{mod} is broadened using a Gaussian kernel, $G(0, \sigma_v)$, to account for the effect of stellar kinematics. The best estimate of the line-of-sight velocity dispersion (LOSVD), σ_v , is assumed to be in the range 0—400 km s⁻¹ and computed iteratively by fitting the narrow (100 Å) wavelength range around the Ca II H&K lines.⁷ The extinction model used in the SSAG (Appendix A) is a two-phase model (Charlot & Fall 2000): birth cloud and diffuse dust, characterised by τ_V and $\mu\tau_V$, respectively. It has been shown by Tojeiro et al. (2007) that due to degeneracies it is not possible to accurately recover these two parameters simultaneously from SED-fitting solutions. Therefore, we model the effect of starlight absorption by the diffuse dust as a single parameter curve $S_\lambda(\mu\tau_V)$, where $\mu\tau_V$ is related to the total extinction in the V-passband as $A_V = 1.086\mu\tau_V$ (single screen model; see M15). The best fitting A_V is assumed to be in the range 0.0—1.5 mag and computed iteratively in a predefined discrete grid designed to ensure the global minimum of χ^2 in Eq. (6). For S_λ in this work we adopt the Charlot & Fall (2000) extinction curve for fitting the mock sample SEDs, which is consistent with the SFH recipe, hence the uncertainties introduced by the starlight absorption model assumed make no contribution in our analysis. For the observed sample, on the other hand, we adopt instead the more conventional Cardelli et al. (1989) extinction curve with a Milky Way parametrization ($R_V = 3.1$). The different treatment of dust in the SSAG and in our fitting model may introduce systematics in our results. The same is true for the time scale of star formation, treated differently in the SSAG than in our fits (see Appendix A). We explore the incidence these differences may have in our results with nearly noiseless mock galaxies in §3.4.

Out of the box, the SSP model flux is expressed in units of $L_\odot \text{Å}^{-1} M_\odot^{-1}$. If F_λ^{obs} is in units of $L_\odot \text{Å}^{-1}$, the coefficients a_{ij}^k in Eq. (8a) are in units of M_\odot . Then $\sum_k a_{ij}^k$ is the estimate of the luminous mass present in the target galaxy, hereafter referred to as the stellar mass. Determining or even defining t_{form} , the formation time of a galaxy, or its metallicity Z , is a difficult task when the integrated spectrum is constantly rejuvenated by young populations in SFGs. $\langle x \rangle_M$ and $\langle x \rangle_L$, the mass- and luminosity-weighted mean values of property x of the stellar populations present in the model galaxy, are used as *proxies* for x , and defined as

$$\langle x \rangle_M = \frac{1}{M_*} \sum_{k=1}^{N_{\text{SSPs}}} a^k x_k, \quad (9a)$$

$$\langle x \rangle_L = \frac{1}{L_{*,r}} \sum_{k=1}^{N_{\text{SSPs}}} a^k F_r^k x_k, \quad (9b)$$

where for simplicity we have dropped the indices ij in a_{ij}^k , and

$$M_* = \sum_{k=1}^{N_{\text{SSPs}}} a^k, \quad (10a)$$

$$L_{*,r} = \sum_{k=1}^{N_{\text{SSPs}}} a^k F_r^k, \quad (10b)$$

are the model galaxy stellar mass and luminosity in the r' -passband, which we use as a reference luminosity, respectively. $\langle x \rangle_M$ is biased towards the value of x of the most massive star-formation event that took place in the target galaxy, while $\langle x \rangle_L$

⁷ This effect is neglected altogether when fitting photometric data.

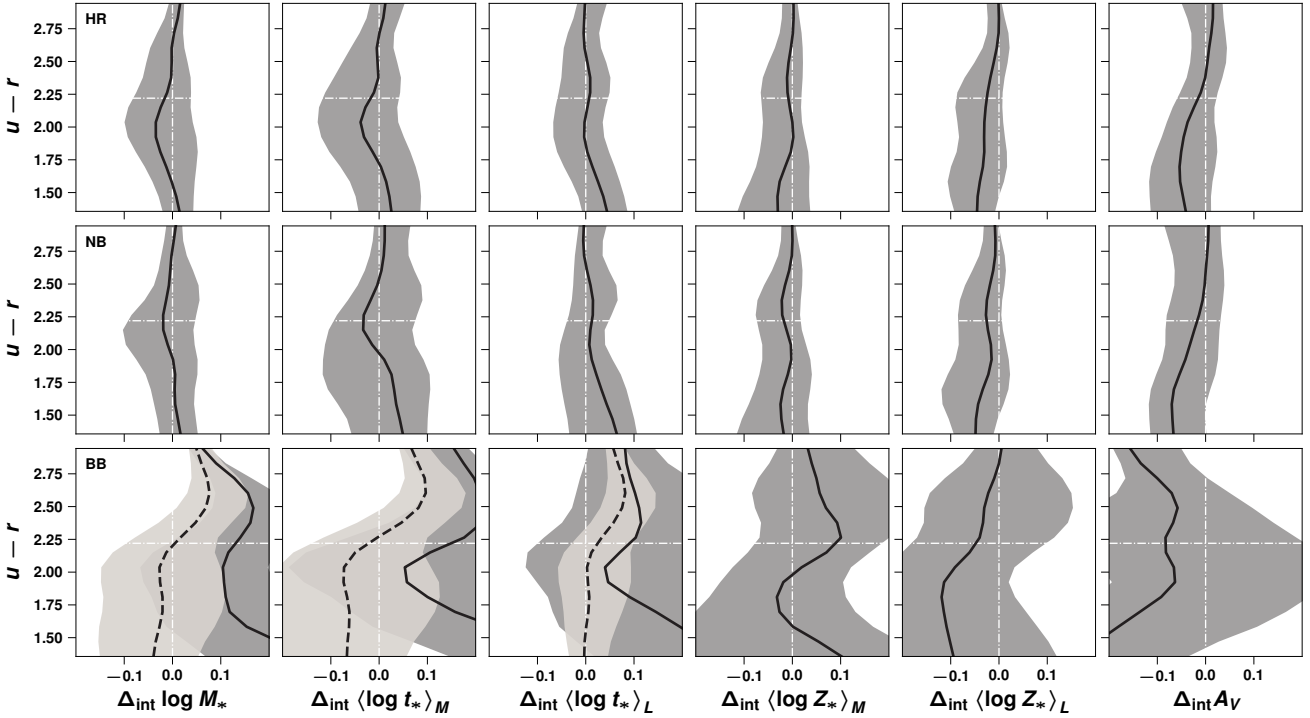


Figure 3. The bias (black line) and precision (grey region) computed for the noiseless data as a function of the $u-r$ galaxy colour at the three spectral resolutions, as indicated in the first column. The behaviour of these residuals at the HR and NB resolutions is notably similar across all the colour range, though it should be noted that NB tends to yield more biased and imprecise results, most notably for SFGs. The BB results are largely biased and imprecise, a weakness that can be overcome by adding relevant information to the fit, as shown by the dashed line, for which the dust extinction and metallicity were fixed to their true values. See text for details.

is biased towards the value of x of the most luminous population dominating the r' -band.

As an entry point to our TTA, after fitting the spectrum of a mock galaxy we define the residual Δx of property x as its *true value* x_{SSAG} subtracted from the value x retrieved from the fit, i. e.,

$$\Delta x \equiv x - x_{\text{SSAG}}. \quad (11)$$

The values of $\log M_*/M_\odot$, $\langle \log t_*/\text{yr} \rangle_M$, $\langle \log t_*/\text{yr} \rangle_L$, Z , and A_V in Table A1 are the *true values* of these properties used in the fits below.

The median(Δx) of the distribution of residuals is used to estimate the *bias* (*accuracy*), and the semi-difference of the 84th and 16th percentiles to estimate the *precision* of our results. We adopt the bias and precision as a measure of the systematic and the random uncertainty in the determination of the physical parameters, respectively. We warn the reader that according to this definition, increasing values of precision characterise less precise results. Moreover these estimates of the bias and precision are lower limits, since results from SED-fitting real observations are prone to suffer from additional uncertainties that for the sake of simplicity are not included in the TTA, e. g., differences between the adopted model stellar ingredients and the actual ingredients present in observed galaxies; the assumed shape and universality of the IMF; instrumental and calibration errors (for a thorough revision see Conroy et al. 2009, 2010, and references therein).

We define the *biasless estimator* \tilde{x} and the *discrepancy* δx of

parameter x as

$$\tilde{x} \equiv x - \text{median}(\Delta x), \quad (12a)$$

$$\delta x \equiv \tilde{x}^{\text{NB}} - \tilde{x}^{\text{HR}}, \quad (12b)$$

respectively, to measure possible differences between the NB photometric and HR spectroscopic estimates of x . In contrast to the residual Δx , the discrepancy δx measures the combined bias and (im)precision arising from the NB and the HR parameter estimations. We note in the case of observed data we cannot compute Δx , therefore we use the same value as for the TTA to provide with a value of \tilde{x} . By removing the predicted bias, we reduce the possible sources of discrepancy to either unpredicted bias (neglected for simplicity in the TTA) and/or random sources of error.

3.4 The impact of the instrumental noise

Maximum likelihood methods are known to produce biased results if the adopted $\mathcal{L}(\{\mathcal{D}_i\} | \mathbf{x})$ does not account for the full data set space (Smith & Hayward 2015). In §2.2 we stated that our motivation behind the different assumptions on the SNR r values at the HR, NB and BB spectral resolutions is to ensure a comparison as independent as possible on the level of noise in the data. We also showed that the adopted values, namely: SNR $r = 20$ for HR spectroscopy, 45 for NB photometry, and 140 for BB photometry, are plausible in the context of current surveys only for bright sources in the local Universe. Given the ill-defined condition of the problem at hand, the overly simplified model assumed as compared to the

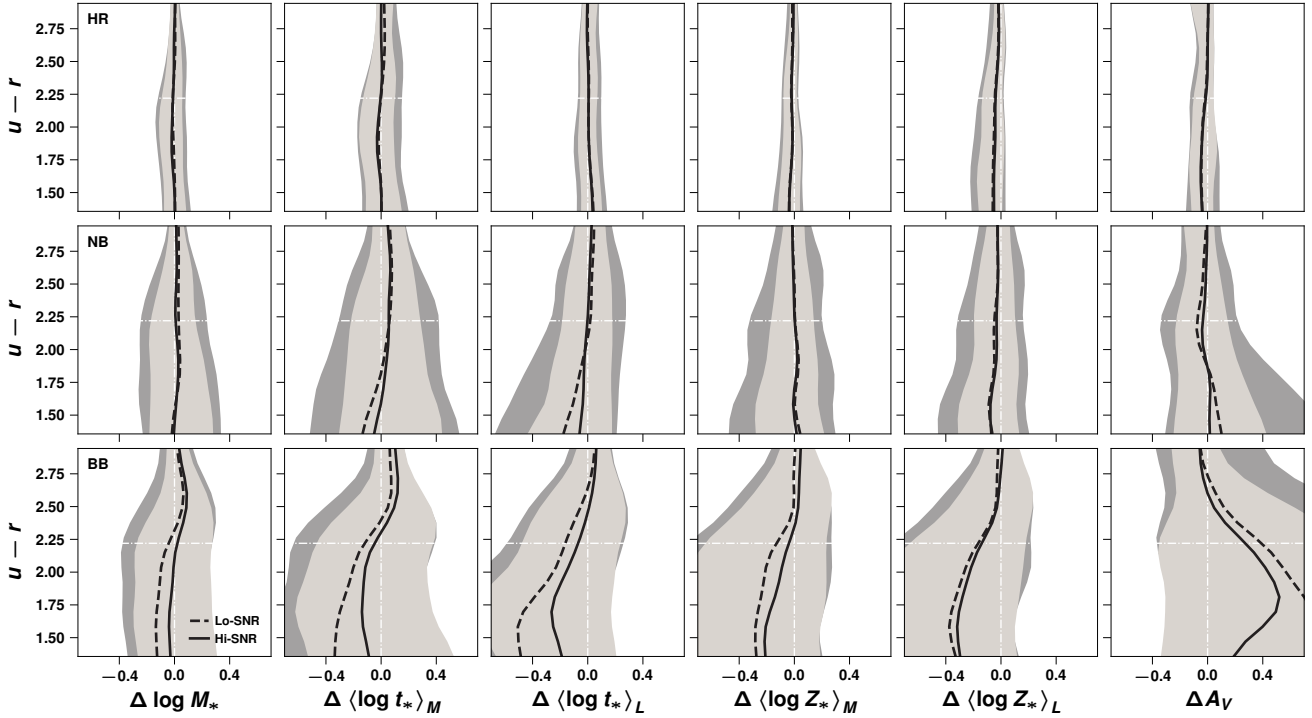


Figure 4. The residuals bias (black lines) and precision (shaded regions) as a function of the $u-r$ colour for fixed values of the SNR $r = 20$ (Lo-SNR) and 45 (Hi-SNR) at the three spectral resolutions, as indicated in the first column. As expected, the precision in the recovered parameters tends to decrease (increase in numerical value) as the SNR r decreases. The bias shows little correlation with the SNR r at high spectral resolution. However, as the spectral resolution decreases, the (absolute) bias at lower values of the SNR r increases. Both effects become more important towards blue SFGs. See text for details.

SSAG recipe, and the dependency of the derived physical properties on data quality (e.g. [Ocvirk et al. 2006](#)), it is worth exploring the impact of instrumental noise in these properties, i.e., the trends in the residuals arising from fitting the data sets as a function of instrumental noise level. For this purpose we use the same SFHs from the mock sample, adopting three fixed values of the SNR, namely: ~ 1000 (essentially noiseless data), 20 (Lo-SNR), and 45 (Hi-SNR), regardless of the spectral resolution. As in the fiducial mock sample, we compute 20 realisations of the noise for the Lo-SNR and Hi-SNR samples. No noise realisation is performed for the noiseless sample. The resulting sample SEDs at the three spectral resolutions are fed to DynBaS, and the recovered physical properties are compared to the true values according to the Eq. (11) in order to compute the intrinsic residuals, $\Delta_{\text{int}}x$, and the conventional residuals Δx for the noiseless and the Lo-, and Hi-SNR samples, respectively.⁸

Fig. 3 shows the behaviour of the intrinsic residuals as a function of the $u-r$ colour for the physical properties studied in this paper. The trends seen in the HR and NB samples show similarities across all the colour range, although the bias (solid line) and the (im)precision (dark grey region) derived from the NB fits are marginally larger, most notably in the case of SFGs. On the other hand, the BB photometry exhibits larger bias and highly imprecise

results for all physical properties. [Pforr et al. \(2012\)](#); [Mitchell et al. \(2013\)](#) have found that BB photometry does not provide clues on the stellar metallicity in a robust manner. They also showed that by excluding stellar properties from the fits (i.e. reducing the x size), the results can be notably improved. In this same spirit, we repeated the BB fits fixing both, the dust extinction and the stellar metallicity, to their corresponding true values for each galaxy in the sample. The resulting bias (dashed line) and precision (light grey region) were computed in this case using the model with $N_{\text{SPPs}} = 2$, which was found to be remarkably better than the $N_{\text{SPPs}} = 3$, as expected given the size of the data set. Interestingly, $\langle \log t_*/\text{yr} \rangle_L$, i.e. the luminosity-weighted-age of the stellar population dominating the galaxy light in the r' -passband, was retrieved with nearly no bias and a precision comparable to NB and HR in the case of SFGs. However, the mass related properties ($\log M_*/M_\odot$ and $\langle \log t_*/\text{yr} \rangle_M$) are both underestimated for the same type of galaxies, most likely due to the outshining effect ([Maraston et al. 2010](#); [Sorba & Sawicki 2015](#)). For the PaGs, the three retrieved properties are overestimated, a sign of the mass-age degeneracy (see discussion in §4.2 for a full analysis). Likewise, Fig. 4 shows the bias for the Lo-SNR (dashed line) and the Hi-SNR (solid line) samples, which in general do not depend strongly on data quality. The precision (dark shaded region for Lo-SNR and light shaded region for Hi-SNR) shows a mild increment (decrement in numerical value) with increasing SNR r , an expected result. It should be noted that these effects show an increasing impact toward lower spectral resolution and bluer SFGs, where the outshining effect is expected to contribute to both the bias and the (im)precision of the results, the

⁸ We remark $\Delta_{\text{int}}x$ and Δx are different in the sense that the former is a measure of the inaccuracy due to the assumed model and methodology alone, whereas the latter measures the combination of both these effects and the contributions of the simulated instrumental noise.

latter contribution being due to the sole presence of the instrumental noise.

It is interesting to note that whatever their origin (the assumed physics and/or the methodology itself), the biases reflect the presence of the several degeneracies between mass, age, metallicity and dust extinction (cf. Fig. 6), and are therefore susceptible of being mitigated once the relevant information in the form of data and/or *a priori* assumptions are taken into account during the spectral fitting, as demonstrated above.

4 FITTING THE MOCK SAMPLE: CRITICAL VIEW

In this section we explore the reliability of SED fitting to infer the physical properties of the target galaxy. We do so by examining the distributions of residuals Δx (Eq. 11), where x denotes any of the following variables, $\log M_*/M_\odot$ (log stellar mass), $\langle \log t_*/yr \rangle_M$ (mass-weighted mean log age), $\langle \log t_*/yr \rangle_L$ (luminosity-weighted mean log age), $\langle \log Z_*/Z_\odot \rangle_M$ (mass-weighted mean log metallicity), $\langle \log Z_*/Z_\odot \rangle_L$ (luminosity-weighted mean log metallicity), and A_V (extinction in the V-band), obtained after fitting with the DynBaS code described in §3.2 the SEDs in our fiducial mock galaxy sample built in §2.2.

The content of the next two subsections is rather technical. The uninterested reader can skip directly to §4.3 where we summarise the main results of §4.1 and §4.2.

4.1 Model Assessment

In the *top frames* of Fig. 5 we show the distributions of residuals for $\log M_*/M_\odot$ and $\langle \log Z_*/Z_\odot \rangle_L$ vs. $\langle \log t_*/yr \rangle_L$ and A_V (colour scale). The *bottom frames* show the corresponding distributions for $\log M_*/M_\odot$ and $\langle \log Z_*/Z_\odot \rangle_M$ vs. $\langle \log t_*/yr \rangle_M$ and A_V . The corresponding 68, 90, and 99 per cent confidence regions of the PDF are shown as contours. The first, second, and third columns refer to HR, NB, and BB, spectral resolutions, respectively. The error cross on each frame is centred at the bias and its length is twice the precision, as defined above. The BB photometry is presented for comparison with similar previous studies (see e.g. Pacifici et al. 2012; Hansson et al. 2012).

In the ideal case, these residual distributions will show highly concentrated PDFs centred at $\Delta x = 0$. Instead, our residual distributions are characterised by the bias \pm precision values listed in Table 1. From this table it is clear that the precision increases (the numerical value decreases) with increasing spectral resolution. In most cases the bias decreases with increasing spectral resolution as well, but unexpectedly there are cases where BB and/or NB photometry seem to outmatch the performance of HR spectroscopy in terms of the bias parameter, e.g., $\Delta \langle \log Z_* \rangle_M$ for All Gals. In the forthcoming sections we will see that such cases are related to the preponderance of instrumental noise over physical effects (e.g. degeneracies). There are regions in Fig. 5 where $\log M_*/M_\odot$, $\langle \log t_*/yr \rangle_L$, $\langle \log t_*/yr \rangle_M$, $\langle \log Z_*/Z_\odot \rangle_L$, $\langle \log Z_*/Z_\odot \rangle_M$, and A_V , are well determined, showing small residuals *simultaneously*. We note that regions of good A_V determination (green symbols, with $-0.08 < \Delta A_V < 0.08$ mag) are usually extended in all frames of Fig. 5, suggesting that A_V is well determined even if other properties are poorly constrained. Furthermore, there are three distinct regions in the distribution of ΔA_V , which are more eloquent at the BB resolution: (i) for most galaxies with $\Delta A_V > 0.30$ mag, $\langle \log t_*/yr \rangle_L$ and $\langle \log t_*/yr \rangle_M$ are underestimated, $\log M_*/M_\odot$ is overestimated,

and $\langle \log Z_*/Z_\odot \rangle_L$ and $\langle \log Z_*/Z_\odot \rangle_M$ are either under or overestimated; (ii) most galaxies with $-0.08 < \Delta A_V < 0.16$ mag show a linear trend with positive slope in the $[\Delta \langle \log t_* \rangle_L, \Delta \log M_*]$ and $[\Delta \langle \log t_* \rangle_M, \Delta \log M_*]$ planes, and with negative slope in the $[\Delta \langle \log t_* \rangle_L, \Delta \langle \log Z_* \rangle_L]$ plane; and (iii) for most galaxies with $\Delta A_V > 0.16$ mag, $\langle \log t_*/yr \rangle_L$ and $\langle \log t_*/yr \rangle_M$ are overestimated, whilst $\langle \log Z_*/Z_\odot \rangle_L$, $\langle \log Z_*/Z_\odot \rangle_M$, and $\log M_*/M_\odot$, are either under or overestimated. These trends are essentially the same in the $[\Delta \langle \log t_* \rangle_L, \Delta \log M_*]$ and $[\Delta \langle \log t_* \rangle_M, \Delta \log M_*]$ planes at the HR spectroscopy and NB photometry resolutions, regardless of the better precision in A_V for the former. However, we note that the fraction of galaxies with overestimated A_V and $\langle \log Z_*/Z_\odot \rangle_L$ shows a tendency to increase with increasing spectral resolution. In the $[\Delta \langle \log t_* \rangle_M, \Delta \langle \log Z_* \rangle_M]$ plane, the smooth dependence with spectral resolution apparent in the $[\Delta \langle \log t_* \rangle_L, \Delta \langle \log Z_* \rangle_L]$ plane breaks into two distinct trends: (i) at the BB resolution there is no evident correlation between $\Delta \langle \log t_* \rangle_M$, $\Delta \langle \log Z_* \rangle_M$, and ΔA_V ; this also holds in the $[\Delta \langle \log t_* \rangle_L, \Delta \langle \log Z_* \rangle_L]$ plane, at least outside the 68 per cent confidence region; and (ii), for HR spectroscopy and NB photometry, the shape of the confidence regions reveals trends among the parameters. The stronger trends lay in the $[\Delta \langle \log t_* \rangle_M, \Delta \log M_*, \Delta A_V]$ volume, and remain strong for all spectral resolutions inside all confidence regions.

4.2 Multiple degeneracies

It is clear that the residuals discussed in §4.1 are correlated with each other in several planes with a remarkable dependence on the wavelength sampling, as signaled by the shape of the confidence regions and the size of the error crosses (see Fig. 5 and Table 2). We interpret these correlations as due to degeneracies in the galaxy properties for different combinations of the galaxy mass, age, metallicity and/or dust extinction. As expected, the stronger correlations appear in the age-metallicity (with the clear exception of BB), age-dust extinction, and age-mass planes. The strong dependence of the precision on the wavelength resolution points towards an interesting result: the dominant degeneracies depend not only on the galaxy colours, but also on the overall stellar population information provided by the data itself, in this case a function of the wavelength resolution.

Fig. 6 presents a quantitative comparison of the different degeneracies apparent in Fig. 5. The vertices of the polygons in Fig. 6 (*left column*) are plotted at a radius equal to the absolute value of the correlation coefficient ρ of the residuals in Table 2, measured in the planes $[\Delta \langle \log t_* \rangle_L, \Delta \langle \log Z_* \rangle_L]$ (right vertex), $[\Delta \langle \log t_* \rangle_L, \Delta A_V]$ (left vertex), $[\Delta \log M_*, \Delta \langle \log t_* \rangle_L]$ (top vertex), and $[\Delta \log M_*, \Delta \langle \log t_* \rangle_M]$ (bottom vertex). The larger the radius, the stronger the degeneracy in the corresponding plane. The lines joining the vertices have no meaning and are shown only to guide the eye. To emphasise the dependence of the degeneracies on the SFH, we show different polygons for SFGs (blue), PaGs (orange), and the whole sample (shaded region). In what follows we will consider a correlation/degeneracy to be relevant if $|\rho| > 0.5$. We will further distinguish between a weak correlation/degeneracy ($0.5 < |\rho| \leq 0.7$), and a strong correlation/degeneracy ($0.7 < |\rho| \leq 1.0$). In this sense the mass-age degeneracy is the strongest, followed by the age-dust extinction degeneracy (with a strong dependence on galaxy type and spectral resolution), and then by the age-metallicity degeneracy (also with a strong dependence on galaxy type).

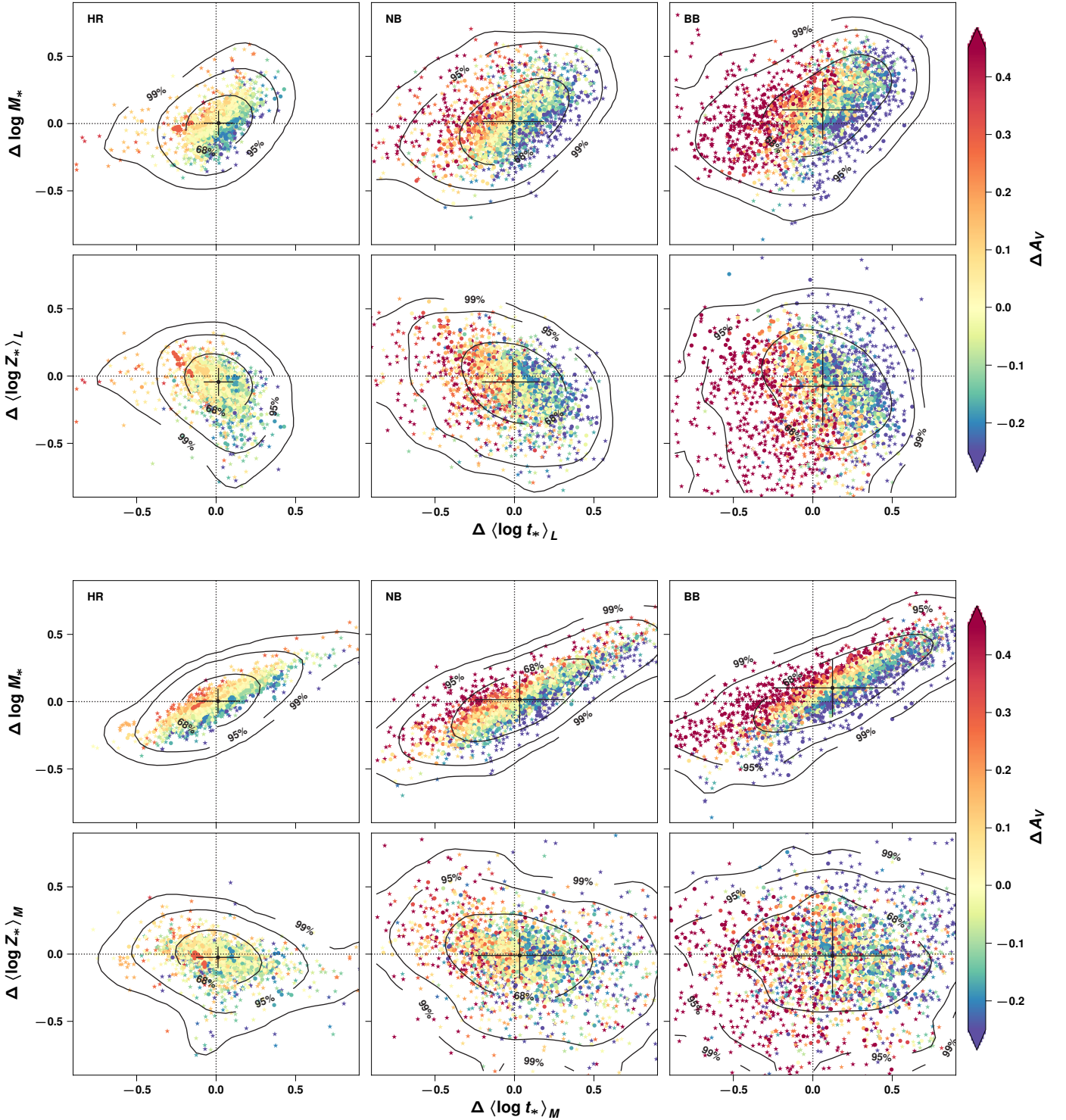


Figure 5. *Top:* The residuals for the several physical properties we discuss in this paper in the framework of the TTA results are shown. Each point represents a galaxy in the mock sample and the shape of the points characterise the galaxy type (SFGs: stars; PaGs: circles). The error cross on each frame is centred at the bias and is twice as large as the precision. The observed trends are interpreted to be due to the several degeneracies, while the different scattering around those trends, as pointed out by the 68, 95 and 99 per cent confidence regions (contours) and the precision, depends on the spectral resolution. *Bottom:* Same as top frame, but for the mass-weighted mean age and metallicity. The strong correlation between stellar mass and mass-weighted age points out the presence of the mass-age degeneracy, regardless of the spectral resolution, whilst the *strength* of the age-metallicity and age-dust extinction degeneracies are clearly correlated with the spectral resolution. SFGs are usually more scattered in all planes than PaGs, i.e., it is more likely to find a SFG beyond the 95 per cent confidence region than a PaG. See text for details.

Table 1. Bias and precision after fitting the mock sample in the different spectral resolutions.

Parameter	Gal. Type	HR		NB		BB	
		bias	precision	bias	precision	bias	precision
$\Delta \log M_*$	SFGs	0.001	0.101	0.011	0.215	0.091	0.264
	PaGs	0.005	0.071	0.019	0.125	0.110	0.140
	All Gals.	0.004	0.092	0.015	0.178	0.102	0.216
$\Delta \langle \log t_* \rangle_M$	SFGs	0.003	0.159	0.002	0.339	0.101	0.454
	PaGs	0.028	0.110	0.065	0.193	0.143	0.192
	All Gals.	0.012	0.139	0.033	0.281	0.124	0.370
$\Delta \langle \log t_* \rangle_L$	SFGs	0.018	0.098	-0.023	0.214	0.047	0.289
	PaGs	0.009	0.086	0.014	0.163	0.081	0.187
	All Gals.	0.015	0.093	-0.010	0.195	0.062	0.255
$\Delta \langle \log Z_* \rangle_M$	SFGs	-0.030	0.093	-0.010	0.212	-0.043	0.320
	PaGs	-0.016	0.060	-0.010	0.126	0.047	0.184
	All Gals.	-0.024	0.080	-0.010	0.171	-0.013	0.280
$\Delta \langle \log Z_* \rangle_L$	SFGs	-0.057	0.119	-0.069	0.202	-0.142	0.318
	PaGs	-0.025	0.074	-0.020	0.131	-0.008	0.184
	All Gals.	-0.044	0.104	-0.044	0.175	-0.076	0.273
ΔA_V	SFGs	-0.032	0.113	-0.014	0.256	-0.032	0.504
	PaGs	-0.008	0.068	-0.020	0.139	-0.018	0.204
	All Gals.	-0.024	0.098	-0.016	0.210	-0.028	0.387

4.2.1 The mass-age degeneracy

The mass:luminosity-weighted-age degeneracy affects mostly PaGs. Its strength varies between $\rho = 0.61$ and 0.72 from BB to NB photometry, showing a negligible weakening towards HR spectroscopy ($\rho = 0.70$). The mass:mass-weighted-age parameters show the strongest degeneracy ($\rho > 0.8$) independently of spectral resolution and galaxy type. This degeneracy is consequence of the logarithmic scale of time evolution of the galaxy integrated optical SED. Above ≈ 1 Gyr, the mass-to-light ratio evolves at essentially the same pace across the optical range, i. e., the shape of the SED is practically time independent within the uncertainties, allowing equally good fits for almost any combination of old stellar populations reaching up to the age of the Universe, with little dependence on the stellar metallicity.

4.2.2 The age-dust extinction degeneracy

For SFGs the age-dust extinction degeneracy decreases as proper age tracers become more prominent with increasing resolution, varying from strong ($\rho = -0.80$) for BB photometry, to weak ($\rho = -0.64$) for NB photometry, to irrelevant ($\rho = -0.47$) for HR spectroscopy. Conversely, PaGs dominated by passively evolving old stellar populations, usually have small amounts of interstellar dust. Features like the 4000 Å-break, prominent in the spectra of PaGs, allow to date these galaxies and break the age-dust extinction degeneracy even at the BB resolution, provided that the reddening by dust is not parallel to the evolution to redder colours with age. Therefore PaGs show a weak age-dust extinction degeneracy with $\rho \sim -0.60$ for BB and NB photometry.

4.2.3 The age-metallicity degeneracy

The luminosity-weighted age and luminosity-weighted metallicity tend to be degenerated for PaGs. Its weak strength marginally in-

creases with resolution from $\rho = -0.60$ for BB, to $\rho = -0.69$ for NB photometry, dropping again to $\rho = -0.66$ for HR spectroscopy. The mass-weighted age:mass-weighted metallicity degeneracy (not shown in Fig. 6) is marginally relevant ($\rho = -0.56$) for HR spectroscopy. At the BB resolution, the luminosity-weighted metallicity is poorly constrained (e. g. Pacifici et al. 2012; Pforr et al. 2012; Hansson et al. 2012; Mitchell et al. 2013). The *simultaneous* absence of age and metallicity tracers in SFGs, in which the young stellar populations may outshine the underlying old ones, increases the imprecision in the determination of these parameters, conspiring to hide the age-metallicity degeneracy at the BB resolution. Conversely, for PaGs the spectral range $\lambda > 7000$ Å provides information on the stellar metallicity, and the age-metallicity degeneracy appears at comparable strength for the three spectral resolutions.

4.3 Summary of Section 4

In §4.1 and §4.2 we made progress in characterising, understanding, and quantifying the ubiquitous degeneracies appearing in galaxy properties derived from SED-fitting. Here we summarise the more important conclusions from these subsections.

(i) The values of the retrieved galaxy properties are usually biased when compared to the known true values, specially at the BB resolution. At the HR spectroscopy and NB photometry resolutions, the biases remarkably diminish, being negligible for PaGs. These systematics may have several origins, namely: physical assumptions in the spectral modelling, the adopted methodology, instrumental effects (e. g., spectral resolution, signal-to-noise ratio) and/or the ability of some galaxies to hide their past SFH from the fitting procedure. We note however, that the goodness-of-fit is always ensured through the existing degeneracies among the retrieved galaxy parameters.

(ii) In fact the biases in the residual distributions and the correlations among them are mainly consequence of the ability of SFGs to

Table 2. Correlation coefficients of residuals versus spectral resolution.

Plane	Gal. type	HR	NB	BB
$[\Delta \langle \log t_* \rangle_L, \Delta \log M_*]$	SFGs	0.48	0.42	0.42
	PaGs	0.70	0.72	0.61
	All Gals.	0.52	0.47	0.45
$[\Delta \langle \log t_* \rangle_L, \Delta \langle \log Z_* \rangle_L]$	SFGs	-0.30	-0.32	0.14
	PaGs	-0.66	-0.69	-0.60
	All Gals.	-0.35	-0.36	0.03
$[\Delta \langle \log t_* \rangle_L, \Delta A_V]$	SFGs	-0.47	-0.64	-0.80
	PaGs	-0.50	-0.59	-0.60
	All Gals.	-0.47	-0.63	-0.77
$[\Delta \langle \log t_* \rangle_M, \Delta \log M_*]$	SFGs	0.88	0.86	0.86
	PaGs	0.87	0.91	0.83
	All Gals.	0.88	0.87	0.85
$[\Delta \langle \log t_* \rangle_M, \Delta \langle \log Z_* \rangle_M]$	SFGs	-0.32	-0.26	0.12
	PaGs	-0.56	-0.46	-0.31
	All Gals.	-0.34	-0.29	0.06
$[\Delta \langle \log t_* \rangle_M, \Delta A_V]$	SFGs	-0.20	-0.39	-0.48
	PaGs	-0.33	-0.43	-0.45
	All Gals.	-0.22	-0.39	-0.48

rejuvenate the stellar population while hiding the underlying older ones (i. e. the outshining effect) and the several well-known degeneracies between stellar mass, stellar age, stellar metallicity, and dust extinction, and as such are susceptible to be mitigated by introducing additional information in the spectral fitting procedure, for instance, in the form of a more comprehensive likelihood and/or with independent determinations of some of the physical properties (as shown in §3.4). The statistical dispersion has its origin on both the outshining effect, and the observational uncertainties added to our mock SEDs.

(iii) The strength of the degeneracies depends heavily on the spectral resolution of the fitted SED and the galaxy type. PaGs exhibit mass-age, age-metallicity, and age-dust extinction degeneracies, with negligible dependence on the spectral resolution. SFGs are more prone to suffer from the age-dust extinction degeneracy, whose strength decreases smoothly with increasing spectral resolution. For SFGs the age-metallicity degeneracy is *hidden* for the BB resolution, becoming progressively stronger with increasing spectral resolution.

(iv) Physical properties retrieved from photometric data show in general larger biases and statistical dispersions than the ones retrieved from spectroscopy, albeit PaGs show comparable biases and degeneracy strength for all spectral resolutions. Interestingly enough, the biases and the degeneracy strengths of the properties derived from HR spectroscopy and NB photometry are strikingly similar, a fact that deserves further exploration.

5 RECOVERED GALAXY PROPERTIES

5.1 Consistency of galaxy property determinations

Given the remarkable resemblance in the strength of the degeneracies affecting NB and HR (§4.2), it is worth exploring how similar or discrepant are the stellar population properties retrieved from both data sets. The objective of this comparison is to quantify the

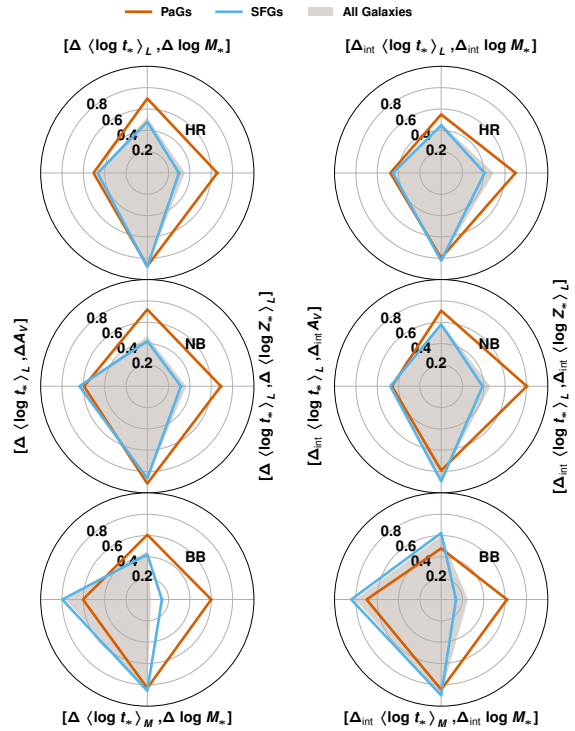


Figure 6. *Left column:* The strength of the age-metallicity, age-dust extinction and mass-age degeneracies are shown as the radii of the polygons, respectively labelled as $[\Delta \langle \log t_* \rangle_L, \Delta \langle \log Z_* \rangle_L]$, $[\Delta \langle \log t_* \rangle_L, \Delta A_V]$, and $[\Delta \langle \log t_* \rangle_M, \Delta \log M_*]$ and $[\Delta \langle \log t_* \rangle_L, \Delta \log M_*]$ at the HR (top), the NB (middle) and BB (bottom) spectral resolutions. The degeneracies affecting PaGs (orange) are almost identical at all SED resolutions. Conversely, the age-dust extinction degeneracy affecting SFGs (blue) shows an important evolution with SED resolution, most notably in the transition between BB and NB, with the latter being marginally equivalent to spectroscopic degeneracies. See text for details. *Right column:* same as left column, but for the intrinsic residuals. The strength of degeneracies affecting HR spectroscopy and NB photometry show little dependence on the presence of instrumental noise. See discussion in §3.4.

differences between both determinations and establish under what circumstances the degree of agreement is better or worse.

The top row of Fig. 7 shows the distributions of the discrepancy δx defined in Eq. (12) for the indicated physical property. The histograms outlined in blue correspond to the mock sample, the shaded histograms to the observed sample. The blue (black) arrow indicates the mean value of δx for the mock (observed) sample. In the bottom frames of Fig. 7 the continuous lines show the mean δx as a function of the galaxy $u - r$ colour, in blue (black) for the mock (observed) sample. The dashed blue line (shaded region) shows the root-mean-square deviation (RMSD) discrepancy for the mock (observed) samples. In Table 3 we list the mean and RMSD δx computed for the SFGs, the PaGs, and the whole mock and observed samples. Observed galaxy data are usually subject to different sources of uncertainty and/or preprocessing due to incomplete model ingredients (e. g. gas emission), which may translate into systematic errors. In particular, the procedure of emission line masking described in §2.1 has removed the Balmer lines carrying information on the stellar content of SFGs in both, HR* and NB* data sets. If these deficiencies in the observed SEDs (as opposed to the mocks) equally propagate from the NB* and the HR* data into

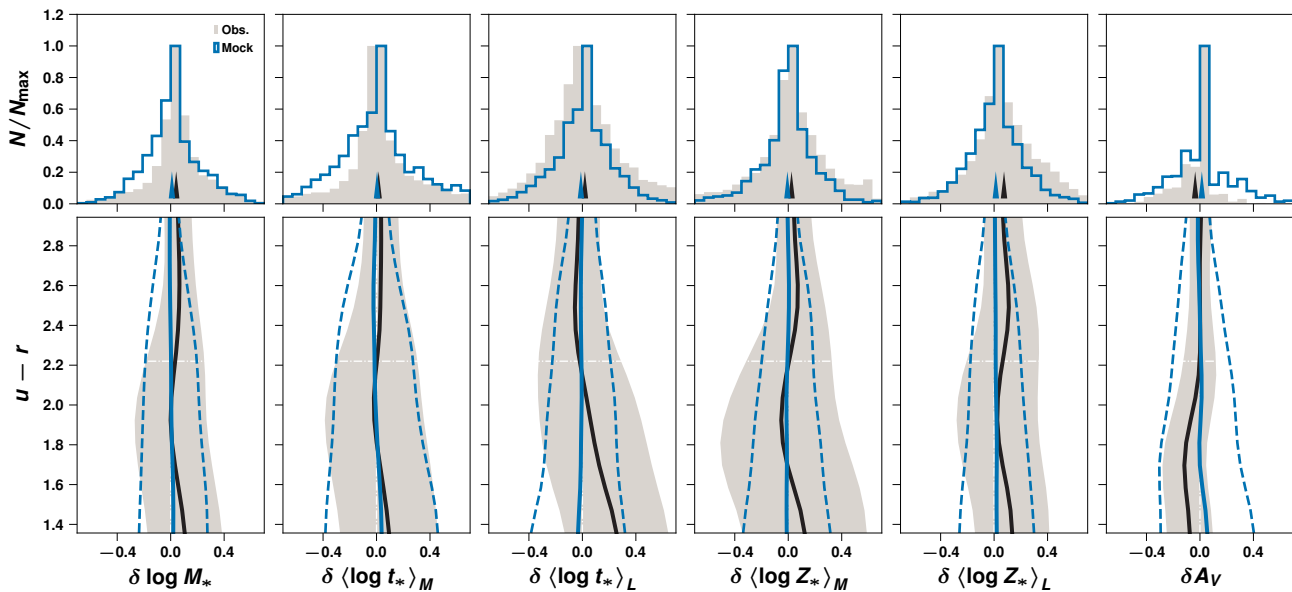


Figure 7. *Top:* Distribution of the discrepancy δx (Eq. 12) for the indicated galaxy parameters in the mock and the observed galaxy samples. *Bottom:* Mean and RMSD discrepancy for the indicated parameters as a function of the $u - r$ colour. Several effects contribute to the discrepancy in the observed sample affecting mainly SFGs. See text for details.

the physical properties and the spectral resolution play minor a rôle, the histograms of the discrepancies for the observed and the mock samples should be similar and highly peaked at $\delta x = 0$, with small RMSD values. In Fig. 7 (top row) this behaviour is observed for $\log M_*/M_\odot$ and $\langle \log t_*/\text{yr} \rangle_M$, regardless of galaxy type (according to the $u - r$ colour, bottom row), and in $\langle \log t_*/\text{yr} \rangle_L$ and A_V for PaGs. The mean discrepancy for $\langle \log t_*/\text{yr} \rangle_L$, $\langle \log Z_*/Z_\odot \rangle_M$, $\langle \log Z_*/Z_\odot \rangle_L$, and A_V for SFGs, exhibits larger departures from a perfect match as can be seen in Fig. 7.

The low values of δx for the parameters mentioned above suggest that these parameters *can be retrieved from NB and HR data with a similar level of accuracy using a non-parametric SED-fitting method, but with a larger precision in the case of HR data*. In the rest of this section we use the galaxy age-metallicity relation (AMR) to explore the veracity of the last statement.

5.2 The G05 spectroscopic AMR as a benchmark

The most accepted theory of galaxy formation in the framework of the Λ CDM cosmology assumes that the onset of star formation in galaxies takes place inside dark matter clumps, which subsequently merge by gravitational attraction with neighbouring clumps in a process dubbed *hierarchical galaxy formation* (White & Frenk 1991; Baugh et al. 1996; Kauffmann 1996). In the local Universe ($z < 0.5$) we only see the aftermath of this process. Population synthesis and spectral modelling techniques allow us to infer the stellar content of galaxies observed by current surveys (e.g. MacArthur et al. 2009; Maraston et al. 2010; Lee et al. 2011; Kriek & Conroy 2013). From such studies several correlations among galaxy properties have emerged (see Renzini 2006, and references therein). The mass-metallicity (MMR, Tremonti et al. 2004) and the age-metallicity (AMR, Worthey 1994) relations are examples of correlations that any model of galaxy formation and evolution should predict. See Cappellari (2016) for a recent review.

The first hint of a relationship between age and metallicity

in galaxies was found in early-type systems using the Lick spectral indices (Gonzalez et al. 1993; Worthey 1994; Bernardi et al. 1998). Later on, G05 presented an assessment of the AMR for a carefully selected sample of galaxies in the local Universe probed by the SDSS, spanning a wide range of galaxy colours which includes SFGs. G05 conclude that the most massive galaxies have on average the older and more metal rich stellar populations, in concordance with previous studies. Likewise, the metallicity of SFGs depends strongly on the stellar mass of the system: on average, smaller galaxies are dominated by younger and lower metallicity populations. In this section we use the G05 results as a benchmark to explore to what extent we can recover their AMR using our SED fitting and parameter recovery methodology. Since our sample was selected to ensure a fair comparison between HR* and NB* over the full range of galaxy colours in the local Universe, a different selection criterium that the one defining the G05 sample, we may expect some differences in the behaviour seen in our determination of the AMR and that of G05 and others (see e.g., Panter et al. 2008; González Delgado et al. 2014). To minimise these differences, we select from our observed sample a subset of 5925 galaxies studied in G05, referred to as the MPA-Garching subset (MGSS, in light blue in Fig. 1).

Since stellar chemical evolution takes place in a generational fashion where massive stars evolve rapidly returning chemically enriched material to the ISM from which the next generations of stars form, whilst less massive stars evolve slowly enough to survive several generations of massive stars, the stellar metallicity is expected to be related to the current SFR (traced by short-lived stars) and to the stellar mass (traced by long-lived stars). Indeed, the theoretical framework describing the large-scale evolution of the metal content locked in stars and present in the interstellar and intergalactic media primarily relate these three physical properties (Tinsley 1980; Madau & Dickinson 2014). Hence most ‘fossil’ studies seeking to shed light on such interplay, jointly relate the AMR to the stellar mass or equivalently the MMR to the current

Table 3. Discrepancy δx between the NB and spectroscopic stellar property determinations.

Parameter	Gal. type	Mock		Observed	
		mean	RMSD	mean	RMSD
$\delta \log M_*$	SFGs	0.016	0.224	0.019	0.271
	PaGs	-0.004	0.150	0.065	0.130
	All Gals.	0.009	0.202	0.041	0.215
$\delta \langle \log t_* \rangle_M$	SFGs	0.019	0.357	0.001	0.369
	PaGs	-0.024	0.230	0.031	0.179
	All Gals.	0.004	0.319	0.016	0.292
$\delta \langle \log t_* \rangle_L$	SFGs	-0.010	0.262	0.087	0.385
	PaGs	-0.012	0.186	-0.052	0.197
	All Gals.	-0.011	0.239	0.019	0.315
$\delta \langle \log Z_* \rangle_M$	SFGs	-0.013	0.251	-0.020	0.444
	PaGs	0.006	0.158	0.071	0.190
	All Gals.	-0.006	0.224	0.025	0.347
$\delta \langle \log Z_* \rangle_L$	SFGs	0.013	0.228	0.043	0.300
	PaGs	0.012	0.159	0.107	0.193
	All Gals.	0.013	0.207	0.074	0.255
δA_V	SFGs	0.022	0.289	-0.068	0.169
	PaGs	-0.001	0.162	-0.002	0.078
	All Gals.	0.014	0.253	-0.036	0.136

SFR (G05; Sánchez et al. 2013; Salim et al. 2014). Nonetheless, in this section we are mainly concerned in providing an objective as possible comparison of the AMRs derived in G05 and in this paper. Therefore we choose to use the $u - r$ colour as a proxy for the mass (Bell & de Jong 2001; Taylor et al. 2010, see also $u - r - \log M_*/M_\odot$ trend in Fig. 9), which, in contrast to the stellar mass, is independent of the spectral analysis method.⁹ Fig. 8(a) shows our derivation of the AMR (grey-shaded area). The 1, 2 and 3 σ confidence regions from the corresponding PDF are shown as contours. The green and dark blue dots and crosses indicate the mean and RMSD values for the galaxies inside five $u - r$ colour bins in the range $1.3 \leq u - r \leq 3.0$ for G05 and this paper, respectively. All these quantities have been computed for the MGSS. The dot-dashed lines in this figure show the slope of the age-metallicity degeneracy computed from the residual correlations shown in Fig. 5, using the SFGs and PaGs subsamples. We adopt the mode as the best fitting parameter estimator of the G05 results for consistency with this paper.

Our AMR spans wider ranges in $\langle \log t_* / yr \rangle_L$ and $\langle \log Z_* / Z_\odot \rangle_L$ than G05's at the $u - r$ -colour blue end of the trends. Furthermore, our estimates of the $\langle \log Z_* / Z_\odot \rangle_L$ show smaller RMSD values for these galaxy types. These results may be suggesting that our methodology is capable of resolving the AMR for SFGs to a higher degree than G05's. However, the unknown true trend and intrinsic scatter in the AMR poses an important difficulty in assessing the veracity of the former statement (see §5.3.3, where we turn back to this issue). Our results imply marginally younger and more metal poor PaGs as compared to the G05 results. Both trends rapidly diverge in $\langle \log t_* / yr \rangle_L$ and $\langle \log Z_* / Z_\odot \rangle_L$ at the transition from PaGs to SFGs. To quantify these differences we define the discrepancy between the G05 and

our results as $\delta_{G05}x \equiv x^{HR^*} - x^{G05}$.¹⁰ Figs. 8(b)–(e) show maps of the mean and RMSD $\delta_{G05}x$ discrepancy for $x = \langle \log t_* / yr \rangle_L$ and $\langle \log Z_* / Z_\odot \rangle_L$. We note in Figs. 8(b,c) that the gradients (the normal vectors to the contours) in the mean $\langle \log t_* / yr \rangle_L$ and $\langle \log Z_* / Z_\odot \rangle_L$ have opposite signs, an evidence of the age-metallicity degeneracy. Figs. 8(d,e) show that the higher RMSD values for $\langle \log t_* / yr \rangle_L$ and $\langle \log Z_* / Z_\odot \rangle_L$ occur in the region occupied by SFGs. From the reddest (PaGs) to the bluest (SFGs) $u - r$ colour bins in Fig. 8(b,c), $\delta_{G05} \langle \log t_* \rangle_L$ varies from -0.15 to < -0.54 , and $\delta_{G05} \langle \log Z_* \rangle_L$ from -0.02 to -0.17 . Our prediction of the systematic effect introduced by the age- and metallicity-related correlations (e.g. the age-metallicity and the age-dust extinction degeneracies) is not enough to explain this amount of discrepancy (cf. mean discrepancy for observed sample in Table 3), although we cannot disregard completely their rôle as a possible source thereof. In Fig. 9 we show the $\delta_{G05} \langle \log t_* \rangle_L$ (top panels) and $\delta_{G05} \langle \log Z_* \rangle_L$ (bottom panels) discrepancies as a function of the physical properties retrieved by DynBaS by fitting the HR* from the MGSS. The big dots represent the mean discrepancy in five bins spanning each physical property range, and are colour-coded according to the mean $u - r$ colour to reflect the predominant galaxy type in each bin. The small dots represent the standard deviation in $\delta_{G05}x$, colour-coded according to the standard deviation in $u - r$ to indicate the galaxy type variation within the bin. The mean tendencies seem to be mainly a consequence of the mass-age and the age-extinction degeneracies, which are not present in G05 determinations. Nonetheless, these degeneracies can explain at most about half the amplitude of $\delta_{G05} \langle \log t_* \rangle_L$. It is interesting to note that $\delta_{G05} \langle \log Z_* \rangle_L$ shows a trend with $\langle \log Z_* / Z_\odot \rangle_L$ but not with $\langle \log t_* / yr \rangle_L$, as would be expected if the age-metallicity degeneracy is affecting the results derived from both data sets in a relative fashion. The strong correlations with galaxy $u - r$ colour, most notably in $\log M_*/M_\odot$ and $\langle \log t_* / yr \rangle_L$, may be indicating that other sources of the $\delta_{G05}x$ discrepancy are needed to explain its amplitude.

5.3 Possible sources of the $\delta_{G05}x$ discrepancy

Since the expected discrepancy (from the TTA) for SFGs does not account for the observed systematics in Fig. 8, this may indicate that one or more additional sources of this discrepancy are operating behind the scene. Here we discuss three possible causes of the discrepancies, namely: (i) the SNR of the observed SEDs; (ii) differences in the SPS models used in the SED fits; and (iii), differences in the nature of the data sets/methodologies adopted to estimate the physical parameters.

5.3.1 The impact of the SNR

The fact that the statistical dispersion in $\delta_{G05}x$ is higher in the locus of SFGs could be pointing to a relation of $\delta_{G05}x$ with the SNR of the SDSS spectra for these galaxies, since on average the SNR is lower in SFG spectra, and there exists a dependency of the bias and precision on the instrumental noise level, as shown in §3.4. In the series of panels in the top two rows of Fig. 10 we show the behaviour of the $\delta_{G05} \langle \log t_* \rangle_L$ and $\delta_{G05} \langle \log Z_* \rangle_L$ discrepancies with the median SNR in several spectral regions: the Ca II H&K

⁹ Although k -corrections were computed using the spectroscopic redshift, those have small amplitudes for the observed sample.

¹⁰ Since the biases from G05 are unknown to us, we cannot define the discrepancy as in Eq. (12). Therefore $\delta_{G05}x$ includes the systematics from both methodologies.

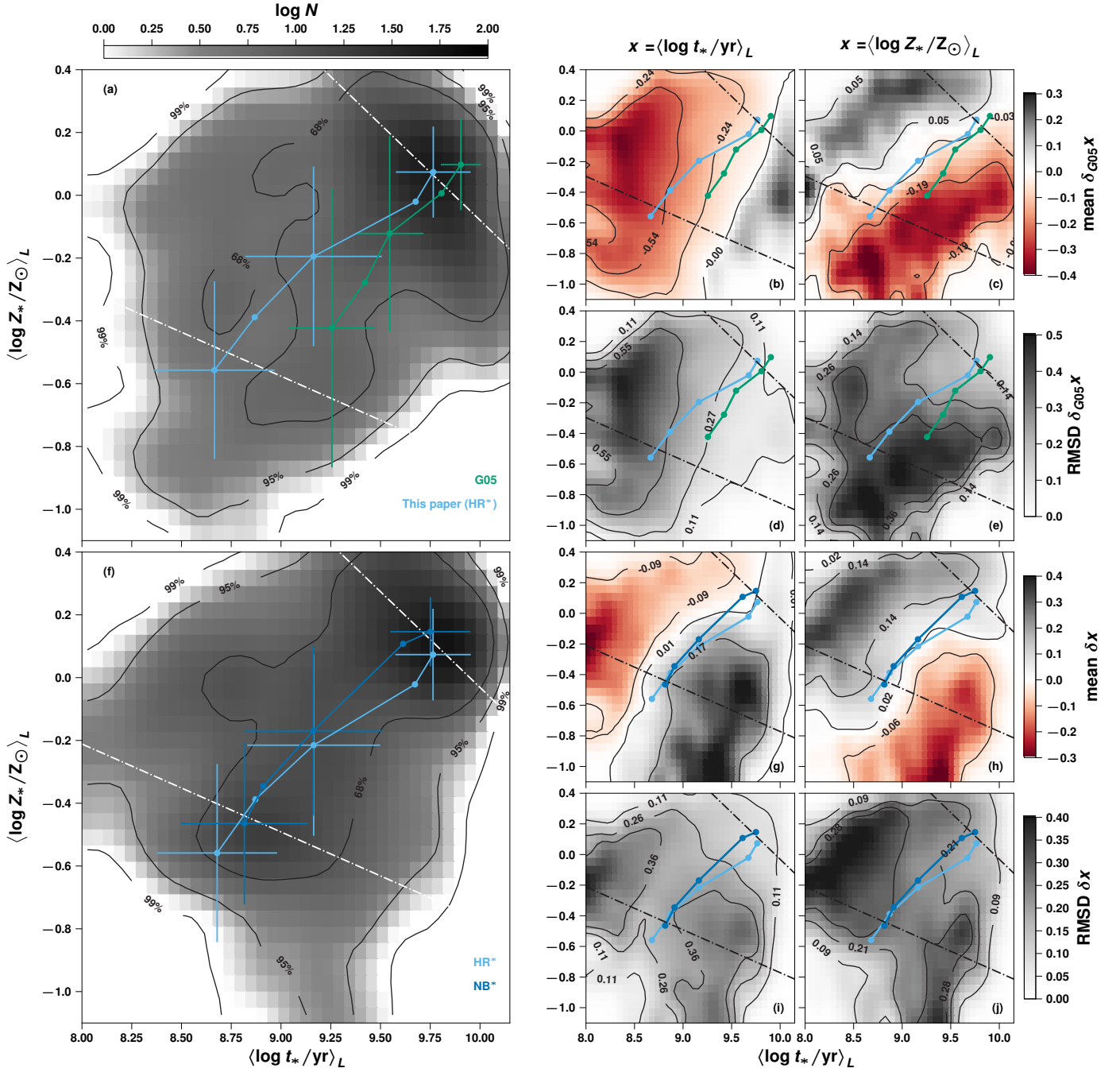


Figure 8. The AMR for our observed galaxy sample determined from HR* and NB*. (a,f) The grey-shaded areas show the AMR for the MGSS retrieved using HR*, and for the complete sample of observed galaxies retrieved using NB*, respectively. The contours enclose the 1, 2 and 3 σ confidence regions of the PDF. (b,d,g,i) Maps of the mean and RMSD discrepancy for $\langle \log t_*/yr \rangle_L$ for the sample in frames (a) and (f), respectively. (c,e,h,j) Same as (b,d,g,i) but for $\langle \log Z_*/Z_\odot \rangle_L$. In frame (a) the green and light blue dots and crosses indicate the mean and RMSD values for the galaxies in the MGSS inside five $u - r$ colour bins in the range $1.3 \leq u - r \leq 3.0$ for G05 and this paper, respectively, derived from HR*. In frame (f) the dark blue and light blue dots and crosses indicate the mean and RMSD values for the galaxies in the complete observed sample, derived from NB* and HR*, respectively. The colour bins are the same as in frame (a). In all frames, the dot-dashed lines show the slope of the age-metallicity degeneracy computed from the residual correlations shown in Fig. 5 using the SFGs and the PaGs subsamples. See text for details.

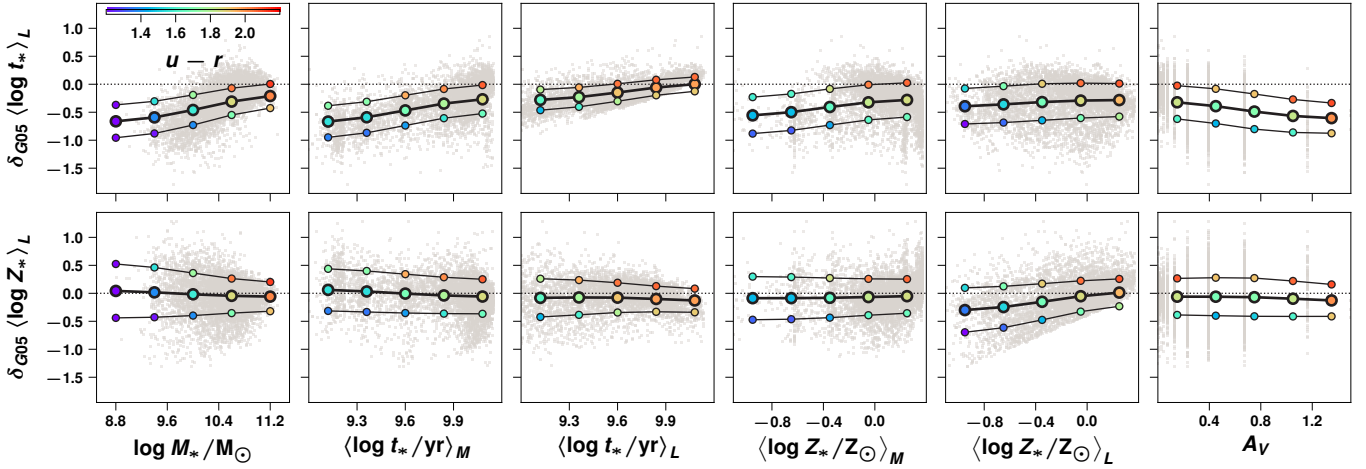


Figure 9. Behaviour of $\delta_{G05} \langle \log t_* \rangle_L$ and $\delta_{G05} \langle \log Z_* \rangle_L$ as a function of the physical properties derived from the HR* fitting. The grey dots show the distribution of all galaxies in the MGSS. The big dots represent the mean $\delta_{G05}x$ in five bins spanning each physical property range, and colour-coded according to the mean $u - r$ colour to reflect the predominant galaxy type in each bin. The small dots represent the standard deviation in $\delta_{G05}x$, colour-coded according to the standard deviation in $u - r$ to indicate the galaxy type variation within the same bins. *Top row:* $\delta_{G05} \langle \log t_* \rangle_L$ shows significant trends with all properties except with $\langle \log Z_*/Z_\odot \rangle_L$. *Bottom row:* $\delta_{G05} \langle \log Z_* \rangle_L$ shows trends only with the $\langle \log Z_*/Z_\odot \rangle_L$ retrieved by DynBaS, as shown in Fig. 8(a). The behaviour of these trends seems to indicate that several degeneracies are at play. See text for details.

lines, the Ca II triplet, the $\lambda > 7000 \text{ \AA}$ (Z-features) region, and the full spectral range covered by the SDSS spectra, computed for the MGSS. The big dots represent the mean discrepancy in five bins spanning each SNR range, and are colour-coded according to the mean $u - r$ colour to reflect the predominant galaxy type in each bin. The small dots represent the standard deviation in $\delta_{G05}x$, colour-coded according to the standard deviation in $u - r$ to indicate the galaxy type variation within the bin. In the Ca II triplet, the Z-feature, and the whole spectral range diagrams, blue SFGs tend to have low SNR and larger departures from $\delta_{G05}x = 0.0$. In fact, $\delta_{G05} \langle \log t_* \rangle_L$ is slightly anticorrelated with SNR, i. e. bluer SFGs have the lowest SNR and the largest $\delta_{G05} \langle \log t_* \rangle_L$, and *vice versa*. Curiously, in the Ca II H&K lines region, $\delta_{G05}x$ is directly correlated with SNR, i. e., the smaller the SNR, the smaller $\delta_{G05}x$, and *vice versa*. In the Ca II H&K line region in the SDSS spectra, the H line is missing while the K line is always present. Since the relative strength of the H&K lines is sensitive to stellar age, this could be a source of systematics introduced in our stellar property estimates from the synthetic narrow-band photometry. We will turn back to this finding in §5.4.

5.3.2 The impact of the stellar library used in the SPS models

G05 used the standard BC03 models whereas we use the BC03xm version of these models described in Appendix A. Both sets of models are based on the Padova 1994 stellar evolutionary tracks (Alongi et al. 1993; Bressan et al. 1993; Fagotto et al. 1994a,b; Girardi et al. 1996). In the optical range of interest to us these models differ only in the stellar library used to build the galaxy SEDs. The STELIB library (Le Borgne et al. 2003) is used in the BC03 models and the MILES library (Sánchez-Blázquez et al. 2006; Falcón-Barroso et al. 2011; Prugniel et al. 2011) in the BC03xm models. The main reason supporting our choice is the very small number of stars with Z away from $1.0 Z_\odot$ in the STELIB library. The number of these stars in the MILES library is much larger (roughly by

a factor of 10), and the spectra have higher resolution and higher SNR than in STELIB. Moreover, BC03 report that the evolutionary tracks and colours are calibrated for $[\text{Fe}/\text{H}] = +0.25$, while the spectral features (including those used by G05) are calibrated using solar abundance models (see Appendix in BC03 for details). As noted by G05, this limitation is particularly important for PaGs, since the BC03 models predict redder colours than observed for $Z \sim 2.5 Z_\odot$. G05 addressed this issue by allowing for negative internal dust extinction to account for this *colour excess* in the models. In their analysis G05 found a strong age-metallicity degeneracy for PaGs. Although we use a different stellar spectral library in our analysis, our results agree with G05's in the presence of this degeneracy (cf. Fig. 6), indicating a library-independent behaviour of this degeneracy (at least for the two stellar libraries being tested).

5.3.3 The impact of the adopted methodology and data set

In this section we evaluate the nature of the discrepancies introduced by the use of different data sets and spectral modelling methodologies in G05 and this paper. G05 inferred stellar properties by simultaneously modelling the five spectral indices $\{\mathcal{D}_i\} = \{\text{D4000}, \text{H}\beta, \text{H}\delta_A + \text{H}\gamma_A, [\text{Mg}_2\text{Fe}], [\text{MgFe}']\}$, suitable for studies of the recent SFH in galaxies. The main motivation behind the G05 choice of the composite $[\text{Mg}_2\text{Fe}]$ and $[\text{MgFe}]'$ spectral indices was that, while providing information of the stellar metallicity, these indices show little dependence on complex chemical abundance patterns such as the α -enhancement, known to be present mainly in early-type galaxies (Conroy et al. 2014). Thus, G05 were able to reduce the number of free parameters, excluding α -enhanced models. In this paper we also adopt SSP models with solar abundance patterns, therefore the α -enhancement is probably a source of systematics given our spectroscopic data set. It should be noted however that, as mentioned before, α -enhanced abundances are expected in galaxies dominated by red old stellar populations, that as shown by the trends in Fig. 8(a) have the smaller $\delta_{G05}x$ discrepancies. We

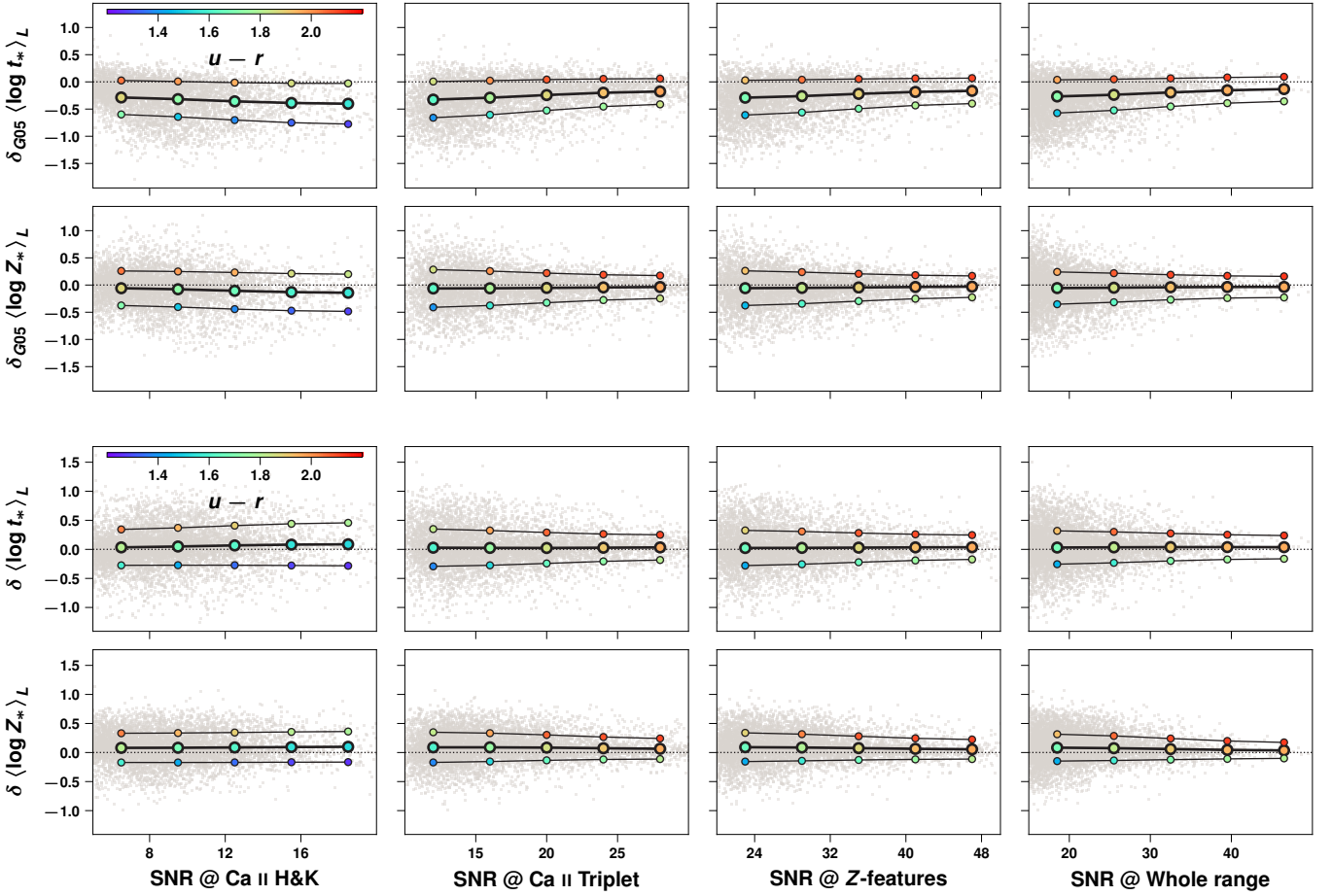


Figure 10. Behaviour of the δ_{G05x} discrepancy as a function of median SNR in four spectral regions, from left to right: Ca II H&K lines, Ca II triplet, $\lambda > 7000 \text{ \AA}$ (Z-feature), and the whole spectral range sampled by the SDSS. The grey dots show the distribution of all galaxies in the MGSS. The big dots represent the mean δ_{G05x} in five bins spanning each SNR range, colour-coded according to the mean $u - r$ colour to reflect the predominant galaxy type in each bin. The small dots represent the standard deviation in δ_{G05x} colour-coded according to the standard deviation in $u - r$ to indicate the galaxy type variation within the same bins. *Top two rows:* $\delta \langle \log t_* \rangle_L$ and $\delta \langle \log Z_* \rangle_L$ for the galaxies in the MGSS, cf. Fig. 8(a). There are no trends with the SNR in any spectral range strong enough to explain the full amplitude of δ_{G05x} observed in SFGs. It should be noted, though, that $\delta_{G05} \langle \log t_* \rangle_L$ is usually larger (in absolute value) towards low-SNR blue galaxies. A correlation between the mean galaxy type (big colour-coded dots) and the SNR is clearly visible in the Ca II triplet, the $\lambda > 7000 \text{ \AA}$, and the whole spectral range, i. e., the smaller the SNR, the bluer the $u - r$ colour, although the galaxy type variation is still large in some cases as indicated by the small colour-coded dots. Interestingly, the trend is inverted in the Ca II H&K lines, i. e., the smaller the SNR, the redder the $u - r$ colour. *Bottom two rows:* $\delta \langle \log t_* \rangle_L$ and $\delta \langle \log Z_* \rangle_L$ for the galaxies in the complete observed sample, cf. Fig. 8(f). The lack of significant trends of $\delta \langle \log t_* \rangle_L$ and $\delta \langle \log Z_* \rangle_L$ with SNR in all the spectral ranges, reveals that the SNR is not a strong source of systematics between the HR* and the NB* results, in agreement with our predictions in §3.4.

can therefore rule out the over abundance of α elements as a major source of systematics in δ_{G05x} . Other possible source of the δ_{G05x} discrepancy may be the nebular infilling of the Balmer lines, which is expected to affect star-forming systems. Likewise, the masking of these lines in our spectroscopic data set is possibly adding to the discrepancies as well. However, as shown below, these effects are probably playing a minor rôle.

G05 use a Bayesian approach to determine the stellar content of galaxies (see §3.1), i. e. they update the prior knowledge on the physical properties of galaxies through their data set (as indicated in Eq. 4), which under the plausible assumption of Gaussian uncorrelated uncertainties yields the likelihood

$$\mathcal{L}(\{\mathcal{D}_i\} | \mathbf{x}) \propto \exp \left\{ - \sum_{i=1}^5 \frac{[\mathcal{D}_i - \mu_i(\mathbf{x})]^2}{2\sigma_i^2} \right\}, \quad (13)$$

where $\mu_i(\mathbf{x})$ represents the proposed model described by the parameters \mathbf{x} . From the equation above we can see that the relative importance of the likelihood in shaping the posterior probability distribution depends on both the size of the data set, in this case $N = 5$, and its quality, $\text{SNR} \sim \mathcal{D}_i / \sigma_i$. For a fixed SNR, the likelihood scales with N , whereas for fixed N the likelihood scales with the SNR. Whenever the data set size is small and/or low-quality, the adopted prior $\pi_0(\mathbf{x})$ dominates the posterior probability distribution. It is therefore worth exploring how the combination of data set plus prior probability distribution in G05 may contribute to the δ_{G05x} discrepancy.

We compute the prior PDF, $\pi_0(\mathbf{x})$, from a version of the SSAG using the same BC03 models as in G05, without including dust extinction nor kinematics effects. In Fig. 11 we show such prior PDF

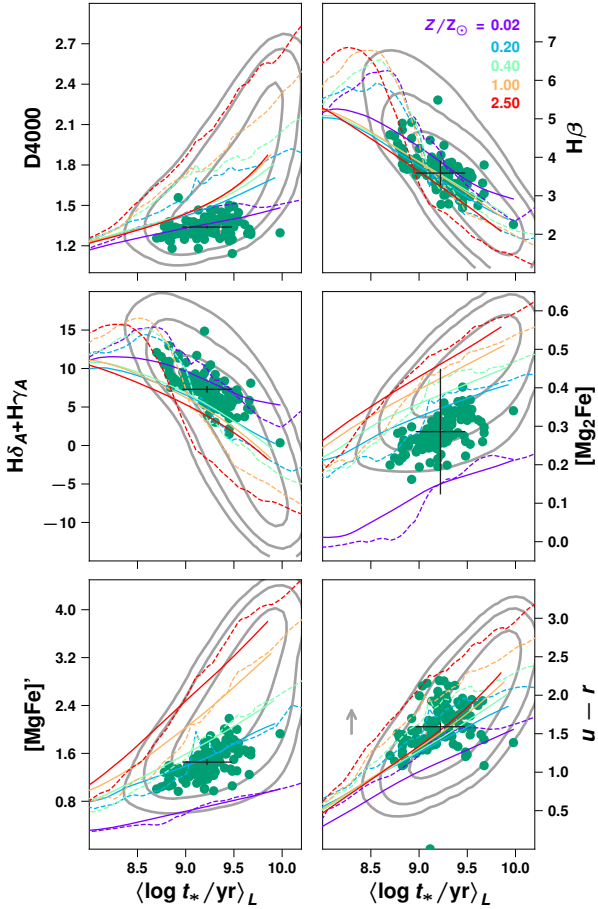


Figure 11. The joint prior PDF in luminosity-weighted mean age computed from the SSAG and projected onto the data set space $\{\mathcal{D}_i\} = \{D4000, H\beta, H\delta_A + H\gamma_A, [Mg_2Fe], [MgFe]'\}$ is shown as contours corresponding to the 1, 2 and 3 σ confidence regions. The projection onto the dereddened stellar continuum as measured by the $u-r$ colour and the reddening vector (arrow) averaged over the SSAG are also shown. The colour-coded lines indicate the indices strengths as a function of the age for the standard BC03 SSP (dashed) and as a function of the luminosity-weighted mean age for $\tau = 5$ Gyr (continuous) models for the different metallicities used in G05. A subset of galaxies from the MGSS for which the $\delta_{G05,x}$ in age and metallicity is large is shown as green dots, and placed in age according to G05 estimates. The cross in each plane is centred at the the mean $\langle \log t_*/\text{yr} \rangle_L$ and the mean index strength and has a length of 2σ , as measured from the joint posterior PDF in $\langle \log t_*/\text{yr} \rangle_L$ reported by G05 (horizontal direction) and the SDSS spectroscopic data (vertical direction). In the planes corresponding to the D4000, $H\beta$, and $H\delta_A + H\gamma_A$ spectral indices the subset of galaxies matches regions of high probability in the prior PDF. Interestingly, in the planes corresponding to $[Mg_2Fe]$ and $[MgFe]'$, the subset of galaxies seems off the high probability locus, favoring old and metal poor stellar populations. See text for details.

projected onto the G05 data set space (grey contours). We show also its projection onto the dereddened $u-r$ colour axis, which we choose as a proxy for the stellar continuum. The arrow represents the averaged reddening vector from the original SSAG recipe, including dust extinction. The age dependency predicted for the indices at the five values of Z in the range $0.02-2.5Z_\odot$ for the standard BC03 SSPs (dashed lines) and for the $\tau = 5$ Gyr models (continuous lines) is shown to highlight the expected boundaries on each plane. At a first glance, those regions with a higher prior

probability density seem to match regions where the density of τ -models is large, an expected result given the SFR parametrization in the SSAG. It is noteworthy though, that there is a lower limit in age at ~ 9 dex, where the prior PDF drops rapidly, despite the fact that SSPs and τ models clearly allow for younger stellar populations.

To see if the behaviour observed in Fig. 11 corresponds with the predictions of G05, we select from the MGSS ~ 100 SFGs with $\langle \log t_*/\text{yr} \rangle_L < 9$ dex (from the HR* fitting) and mean $\delta_{G05} \langle \log t_*/\text{yr} \rangle_L, \delta_{G05} \langle \log Z_*/Z_\odot \rangle_L \approx -0.6, -0.2$. To mitigate the importance of degeneracies in the kinematic effects and the nebular infilling, we also require this subset of galaxies to belong to the lowest percentile of the LOSVD distribution ($\sigma_v < 50 \text{ km s}^{-1}$), and we measure the spectral indices from the best fitting model SED, both retrieved by DynBaS from the HR* spectroscopy. In Fig. 11 these galaxies are represented by the green dots, located in age according to G05's results. The cross in each plane is centred at the subset mean age and mean index strength and have a length of 2σ according to G05 estimates and SDSS measurements in the horizontal and the vertical directions, respectively. It is worth noting that these galaxies are located near the locus of the younger stellar content in the prior PDF (~ 9 dex) projected onto the D4000, $H\beta$, and $H\delta_A + H\gamma_A$ indices, whilst in the $[Mg_2Fe]$ and $[MgFe]'$ projections, the same galaxies require slightly younger populations and/or higher index strengths in those spectral features to match the same locus. This result could be indicating a major influence of the prior PDF in determining the stellar age. In the $u-r$ colour projection, adding to the prior PDF the averaged colour excess indicated by the arrow seems to be enough to make the green dots fall onto the high probability locus, indicating that this colour index may not provide further information to the posterior PDF. We remark, however, that the prior set by the SSAG is probably different from the one adopted by G05, and such differences may well affect the conclusions we can draw from the behaviour seen in Fig. 11.

To test if this is the case, we compute the posterior PDF by updating the knowledge about x enclosed by the SSAG through the likelihood in Eq. (13), where $\mu_i(x)$ represents the SSAG's predictions of the same spectral indices as in G05. The distribution of the joint posterior PDF modes in $\langle \log t_*/\text{yr} \rangle_L$ and $\langle \log Z_*/Z_\odot \rangle_L$ for each galaxy is shown in Fig. 12 (blue), along with the results from G05 (green), and those we derived in this paper using DynBaS (grey). Despite the aforementioned difference in the prior PDFs, we are able to retrieve trends in good agreement with G05's, suggesting to some extent a degree of independency of the posterior PDF on the adopted prior, regardless of the data set. However, the lack of stellar populations younger than 9 dex in G05, but present in the DynBaS results, could be pointing toward a limitation in the parameter space sampling, according to the results presented in Fig. 11. Incidentally, the results derived from the posterior PDF may be interpreted as either that the indices D4000, $H\beta$, and $H\delta_A + H\gamma_A$ place too strong constrains on stellar age given their typically high SNR, therefore biasing the metallicity estimates through the age-metallicity degeneracy, or that the $[Mg_2Fe]$ and $[MgFe]'$ indices are too weak to break this degeneracy in SFGs.

5.4 The AMR determined from NB* photometry

In Fig. 8(f) we show the AMR inferred from our complete observed sample using the NB* fits (grey-shaded area and contours). The light blue dots and crosses indicate the mean and RMSD values for the galaxies in this sample in the same five $u-r$ colour bins of Fig. 8(a), computed using HR*. The dark blue dots and crosses show the AMR for the same galaxies derived from NB*.

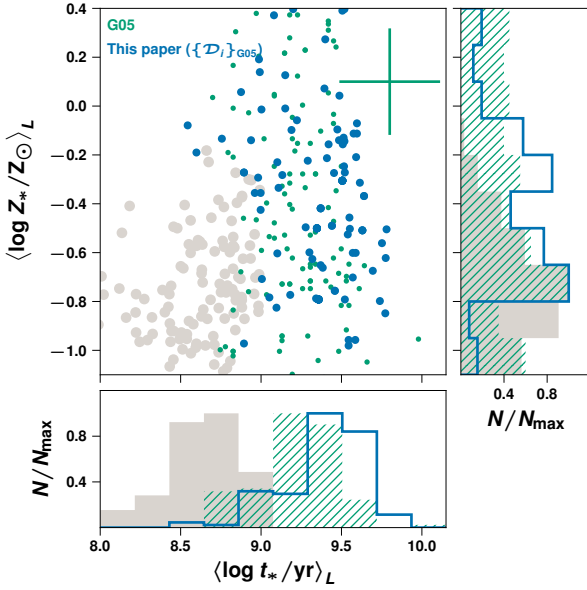


Figure 12. The mode of the posterior PDF for each galaxy from the subset of ~ 100 MGSS galaxies, computed using the SSAG as prior, is shown in blue (labelled $\{\mathcal{D}_i\}_{G05}$). The results from **G05** (green) are for comparison, demonstrating the same general behavior: high dispersion in metallicity, with a tendency towards old and metal-poor stellar populations. The error cross represents the typical 2σ range in age and metallicity in **G05** estimates. These results demonstrate that the derived galaxy properties are, to some extent, independent of the chosen prior distribution, provided that the SSAG and **G05** adopt different priors. The results from this paper are also shown (grey) to illustrate the discrepancy for this particular subset of galaxies. See text for details.

Figs. 8(g)–(j) show the maps of the mean and RMSD δx discrepancy in $\langle \log t_*/\text{yr} \rangle_L$ and $\langle \log Z_*/Z_\odot \rangle_L$. Even though the main trends between the photometric and spectroscopic results are essentially the same, cf. Figs. 8(a) and 8(f), a closer inspection of the PDF (grey-shaded regions) reveals some differences worth discussing. The PaGs in the two redder bins seem to have migrated towards higher metallicities and slightly younger ages in the NB* AMR with respect to their position in the spectroscopic AMR. This is consistent with our findings in §4, where we showed that for this type of galaxies the age-metallicity degeneracy is more pronounced in the NB* than in the HR* results, although the systematics found in the TTA cannot fully account for the observed discrepancy. In the SFG region, the HR* results include a population of young and metal-poor galaxies, reaching $\langle \log t_*/\text{yr} \rangle_L \sim 8.5$ and $\langle \log Z_*/Z_\odot \rangle_L \sim -0.8$ at the extremes of the bluest bin, which is absent in the NB* prediction. Instead, there are two groups of galaxies in the NB* AMR not present in the HR* AMR: an extremely young and relatively metal-rich subpopulation, ($\langle \log t_*/\text{yr} \rangle_L \sim 8$, $\langle \log Z_*/Z_\odot \rangle_L \sim -0.3$), and a slightly older and extremely metal-poor subpopulation, ($\langle \log t_*/\text{yr} \rangle_L > 9.2$, $\langle \log Z_*/Z_\odot \rangle_L < -1.0$). In Figs. 8(g)–(h) we can see that the gradient vectors in the mean maps of δx follow the age-metallicity degeneracy direction. The larger discrepancies are found around (8.0, -0.2), (9.3, -1.1), and (9.6, -0.5). Such regions have also the larger statistical dispersion (RMSD, Figs. 8(i)–(j)). None of these discrepancies were predicted in the TTA. Since the models and the method are the same for both data sets, this may indicate that the origin of this discrepancy is related to observational artefacts.

In the bottom two rows of Fig. 10 we show the behaviour of $\delta \langle \log t_* \rangle_L$ and $\delta \langle \log Z_* \rangle_L$ with SNR in several spectral ranges for the NB* results. In general, SFGs have the lowest SNR at the Ca II triplet, the Z-features, and the whole spectral ranges, and show the highest discrepancy in $\delta \langle \log t_* \rangle_L$ and $\delta \langle \log Z_* \rangle_L$. The insensitivity of $\delta \langle \log t_* \rangle_L$ and $\delta \langle \log Z_* \rangle_L$ to the median SNR in all the spectral ranges shown, reveals that the data quality (as measured by the SNR) is a not strong source of systematics between the HR* and the NB* results. Therefore, the combination of the lower spectral resolution of NB photometric data and the invisibility of some age/metallicity-sensitive spectral features are likely the major sources of systematics. Such is the case of the masking of the Balmer lines due to emission and the missing pixels for imperfect spectroscopic observations. Particularly incident is the fact that the Ca II H line, part of the Ca II H&K spectral index and a stellar age tracer, is missing from spectroscopic observations. In the blue region of the SED ($< 4000 \text{ \AA}$) we found that this lack produces a strong systematic offset in the selected best fitting model, generally bluer than the observed SED. This also explains the opposite behaviour of the discrepancies in stellar age and stellar metallicity with SNR in the Ca II H&K spectral range: the higher the SNR around this feature, even if incomplete, increases its relative importance in the SED fit (since $\chi^2_\lambda \propto 1/\sigma_\lambda^2$) and the chances of mismatching the corresponding spectral fitting result. Moreover, the lack of sensitivity to stellar metallicity of the reddest region of the SED ($> 7000 \text{ \AA}$), due to missing pixels, contributes to the observed systematic discrepancy in $\langle \log Z_*/Z_\odot \rangle_L$ and $\langle \log Z_*/Z_\odot \rangle_M$. This last fact is specially important for PaGs, for which the photometric stellar metallicity estimates rely strongly on the availability of the reddest region of the optical SED.

In our estimations from both HR* and NB* data, galaxies dominated by < 1 Gyr stars are relatively rare, adding up to ~ 25 per cent in the observed sample. In the SSAG, presumably representing a similar prior knowledge as that used in **G05**, around 20 per cent of the galaxies are dominated by such young populations and are characterised by a specific SFR, i.e. the fraction of newly formed stellar mass per unit time averaged over a given time scale, $\text{sSFR} \equiv \text{SFR}/M_* \approx 0.18 \text{ Gyr}^{-1}$. Given their remarkable absence from the **G05** results, the occurrence of these galaxies is worth exploring in the context of current galaxy formation simulations. Recently, Guo et al. (2016) presented a comprehensive comparison of three widely known simulations in the literature (see references therein). The predicted distribution of the sSFR for galaxies with $\log M_*/M_\odot < 9.75$ (blue SFGs in our MGSS) is quite similar at $z = 0$ among all explored simulations, characterised by a median around ~ 0.06 – 0.16 Gyr^{-1} , a long high-probability and slowly declining tail toward lower values and a rapid drop toward upper values. This suggest that galaxies with important recent star formation events, dominated by young stellar populations, may be in fact rare in the nearby Universe. Indeed, the bulk of mass the budget seems to be in the form of old metal-rich stars, albeit in the lowest mass bin young stars probably dominate (Baldry et al. 2004; Conzelmann 2006). This is also consistent with the reviewed references by Madau & Dickinson (2014), from which estimations using UV/IR calibrations span $\text{sSFR} \sim 0.10$ – 0.30 Gyr^{-1} in the local Universe. From the MGSS, these galaxies ($\log M_*/M_\odot < 9.75$ from **G05** estimations) are characterised by the following distributions, accord-

ing to our NB* (G05) results:

$$\begin{aligned} \log M_*/M_\odot &\approx +9.69^{+0.27}_{-0.34} \quad \left(+9.63^{+0.09}_{-0.23}\right), \\ \langle \log t_*/\text{yr} \rangle_L &\approx +8.76^{+0.28}_{-0.93} \quad \left(+9.08^{+0.26}_{-0.26}\right), \\ \langle \log Z_*/Z_\odot \rangle_L &\approx -0.42^{+0.25}_{-0.33} \quad \left(-0.58^{+0.75}_{-0.51}\right). \end{aligned}$$

From the simulations explored by Guo et al., galaxies in this stellar mass range at $z = 0$, span a stellar metallicity range as wide as $\log Z_*/Z_\odot \approx -0.73$ — 0.07 , in agreement with our results and those from G05. Nonetheless, the predictions from galaxy formation simulations, specially in the case of low stellar mass galaxies, are still highly contradictory among different implementations, most likely due to uncertainties regarding the assumed physics of the star formation, the chemical enrichment and the regulating processes thereof (see Guo et al. 2016; Naab & Ostriker 2017). As a matter of fact, the intrinsic scatter and the relative importance of the global and local phenomena in shaping the AMR/MMR are subjects of an active debate (e. g. Lara-López et al. 2010; Rosales-Ortega et al. 2012; Sánchez et al. 2013; González Delgado et al. 2014). In the near future the results from the spectral fitting will continue to prove valuable to both, fossil studies and numerical simulations, in our path towards unraveling the nature of these relations in star-forming systems.

6 SUMMARY AND CONCLUSIONS

We have explored the consistency among the physical properties of galaxies retrieved from SED-fitting data sets of different spectral resolution and quality. We perform our tests on two different samples of galaxy spectra. For the first sample we draw 7k high quality spectra from the SDSS-DR7 including both PaGs ($u - r > 2.22$ mag) and SFGs ($u - r \leq 2.22$ mag). More than 80 per cent of these galaxies are in common with the sample studied by G05 and define the MGSS. For the second sample we build a set of 2680 mock galaxy spectra representing the local Universe as realistically as possible by combining a randomly selected collection of galaxy SFH's from C12 with the BC03xm SPS models. For the mock sample we simulate broad-band (BB) and narrow-band (NB) observations across the optical wavelength range, using the $u'g'r'i'z'$ and the 56 J-PAS passbands response functions, respectively. In the case of the observed sample a subset NB* of only ~ 40 can be synthesized from the SDSS spectra, due to instrumental artefacts. We use the DynBaS code to fit the high-resolution (HR) spectra in both samples, as well as their BB, NB and NB* versions. From each spectral fit, we compute the stellar mass, the mass- and luminosity-weighted age and metallicity, and the dust extinction for the associated galaxy. For the galaxies in the mock sample we know the true value of each of these properties.

The galaxy properties retrieved from fitting the mock sample at the BB resolution are usually biased. At the NB and HR resolutions the biases are practically nil for PaGs and show a slight increase for the bluer SFGs. Such biases are produced at several levels by the modelling methodology, the instrumental effects, the assumed physics and the ability of some galaxies to hide their past SFH, and they manifest through the several well-known degeneracies between stellar mass, stellar age, stellar metallicity, and dust extinction. The statistical dispersion, on the other hand, arises from our simulation of observational effects through the addition of random noise to the fitted mock SEDs, and from the ability of SFGs to rejuvenate their stellar population. In fact, our results indicate

that the instrumental noise is relatively unimportant as a source of the bias at the HR and NB spectral resolutions, but becomes more important towards blue SFGs and at lower spectral resolutions. We find that the strength of the several degeneracies is a function of the spectral resolution and galaxy type, albeit exhibits little dependence on the level of instrumental noise. PaGs show comparable biases and strong presence of the mass-age, age-metallicity, and age-dust extinction degeneracies for all spectral resolutions. SFGs, on the other hand, are more prone to show the age-dust extinction degeneracy at the BB resolution rather than at the HR, whilst the age-metallicity degeneracy is hidden at the BB resolution and appears progressively with increasing spectral resolution. In general, the biases and degeneracy strengths resulting from the HR and NB fits are comparable.

The direct comparison of the parameters derived from HR* spectroscopy and NB* photometry for the galaxies in the observed sample shows trends with galaxy colour. For PaGs these trends are consistent with the relative presence of the age-metallicity, the mass-age, and, to a lesser extent, the age-dust extinction degeneracies. For SFGs the trends are consistent with the relative presence of the mass-age and the age-dust extinction degeneracies, and the absence of the age-metallicity degeneracy. The existence/absence of the degeneracies is consistent with the results from the mock sample fits, but the systematic discrepancies expected from the mock sample results are not large enough to account for the discrepancies in the results derived from the observed samples. This suggests that additional sources of systematic discrepancies between the NB* photometry and the HR* spectroscopy results, not accounted for in the mock galaxy modelling, are at play. We evaluated two possible sources: the decreasing SNR in the lower surface brightness regions of SFGs, and the lack of stellar age and metallicity indicators in the spectral regions of interest affecting both PaGs and SFGs. The latter is propagated from the artefacts in HR* data to the NB* synthetic photometry, showing the importance of sampling in relevant wavelength ranges to provide with reliable estimates of the stellar contents in galaxies. Indeed the discrepancies in the parameters determined from NB* photometry and HR* can be understood as due to these additional sources of systematics.

Using the G05 results for the MGSS as a benchmark to compare with our spectroscopic results, we show *the rôle of the prior PDF in shaping the posterior PDF when modelling small and/or low-SNR data sets, and how it may introduce biases not accounted for in a Bayesian framework*. Despite the aforementioned sources of uncertainty, the same AMR trends can be drawn using our methodology and the G05's, both consistent with more recent results in the literature (e. g., Panter et al. 2008; González Delgado et al. 2014). In general, the distributions of the stellar mass and the mass-weighted age determined from HR* spectroscopy and NB* photometry are consistent across the full colour range. The luminosity-weighted age and dust extinction distributions are consistent only for PaGs. The statistical dispersion in the parameters derived for PaGs from HR* and NB* data are consistent with, or at least comparable to, the expected dispersion from the mock sample fits. We conclude that *NB photometry can provide the stellar mass, stellar mass- and luminosity-weighted age, and dust extinction to an accuracy similar to spectroscopic data sets, however the precision provided by the HR data sets still outmatches that from NB photometry*, an effect that may be crucial in studies of distant galaxies.

ACKNOWLEDGMENTS

We thank an anonymous referee for very useful comments that made this paper more clear, a bit longer, but hopefully more useful to the interested reader. Special thanks to Cecilia Mateu for insightful discussions and useful suggestions. AMN acknowledges support from the Sociedad Mexicana de Física through its Program México-Centro América y el Caribe para el Avance de la Ciencia, la Tecnología y la Innovación, and thanks the Centro de Investigaciones de Astronomía (CIDA) for a graduate student grant. AMN also thanks the warm hospitality of the Instituto de Radioastronomía y Astrofísica of the National Autonomous University of México (IRyA, UNAM) and the Centro de Estudios de Física del Cosmos de Aragón (CEFCA) during part of this research. GB acknowledges support for this work from UNAM through grant PA-PIIT IG100115.

Funding for the SDSS and SDSS-II has been provided by the Alfred P. Sloan Foundation, the Participating Institutions, the National Science Foundation, the U.S. Department of Energy, the National Aeronautics and Space Administration, the Japanese Monbukagakusho, the Max Planck Society, and the Higher Education Funding Council for England. The SDSS Web Site is <http://www.sdss.org/>.

The SDSS is managed by the Astrophysical Research Consortium for the Participating Institutions. The Participating Institutions are the American Museum of Natural History, Astrophysical Institute Potsdam, University of Basel, University of Cambridge, Case Western Reserve University, University of Chicago, Drexel University, Fermilab, the Institute for Advanced Study, the Japan Participation Group, Johns Hopkins University, the Joint Institute for Nuclear Astrophysics, the Kavli Institute for Particle Astrophysics and Cosmology, the Korean Scientist Group, the Chinese Academy of Sciences (LAMOST), Los Alamos National Laboratory, the Max-Planck-Institute for Astronomy (MPIA), the Max-Planck-Institute for Astrophysics (MPA), New Mexico State University, Ohio State University, University of Pittsburgh, University of Portsmouth, Princeton University, the United States Naval Observatory, and the University of Washington.

REFERENCES

- Abazajian K. N., et al., 2009, *ApJS*, 182, 543
- Alongi M., Bertelli G., Bressan A., Chiosi C., Fagotto F., Greggio L., Nasi E., 1993, *A&AS*, 97, 851
- Baldry I. K., Glazebrook K., Brinkmann J., Ivezić Ž., Lupton R. H., Nichol R. C., Szalay A. S., 2004, *ApJ*, 600, 681
- Bastian N., Covey K. R., Meyer M. R., 2010, *ARA&A*, 48, 339
- Baugh C. M., Cole S., Frenk C. S., 1996, *MNRAS*, 283, 1361
- Bell E. F., de Jong R. S., 2000, *MNRAS*, 312, 497
- Bell E. F., de Jong R. S., 2001, *ApJ*, 550, 212
- Benítez N., 2000, *ApJ*, 536, 571
- Benítez N., et al., 2014, preprint, ([arXiv:1403.5237](https://arxiv.org/abs/1403.5237))
- Bernardi M., Renzini A., da Costa L. N., Wegner G., Alonso M. V., Pellegrini P. S., Rité C., Willmer C. N. A., 1998, *ApJ*, 508, L143
- Bevington P. R., Robinson D. K., 2003, *Data Reduction and Error Analysis for the Physical Sciences*. McGraw-Hill
- Bressan A., Fagotto F., Bertelli G., Chiosi C., 1993, *A&AS*, 100, 647
- Brinchmann J., Charlot S., White S. D. M., Tremonti C., Kauffmann G., Heckman T., Brinkmann J., 2004, *MNRAS*, 351, 1151
- Bruzual G., Charlot S., 2003, *MNRAS*, 344, 1000
- Cabrera-Ziri I., Mejía-Narváez A., 2014, *Synthetic Spectral Atlas of Galaxies (SSAG)*
- Cabrera-Ziri I., et al., 2016, *MNRAS*, 457, 809
- Cappellari M., 2016, *ARA&A*, 54, 597
- Cardelli J. A., Clayton G. C., Mathis J. S., 1989, *ApJ*, 345, 245
- Castellano M., et al., 2014, *A&A*, 566, A19
- Chabrier G., 2003, *PASP*, 115, 763
- Charlot S., Fall S. M., 2000, *ApJ*, 539, 718
- Chen Y.-M., et al., 2012, *MNRAS*, 421, 314
- Chevallard J., Charlot S., 2016, *MNRAS*, 462, 1415
- Cid Fernandes R., Mateus A., Sodré L., Stasińska G., Gomes J. M., 2005, *MNRAS*, 358, 363
- Cid Fernandes R., et al., 2013, *A&A*, 557, A86
- Coelho P. R. T., 2014, *MNRAS*, 440, 1027
- Conroy C., 2013, *ARA&A*, 51, 393
- Conroy C., Gunn J. E., 2010, *ApJ*, 712, 833
- Conroy C., Gunn J. E., White M., 2009, *ApJ*, 699, 486
- Conroy C., White M., Gunn J. E., 2010, *ApJ*, 708, 58
- Conroy C., Dutton A. A., Graves G. J., Mendel J. T., van Dokkum P. G., 2013, *ApJ*, 776, L26
- Conroy C., Graves G. J., van Dokkum P. G., 2014, *ApJ*, 780, 33
- Conselice C. J., 2006, *MNRAS*, 373, 1389
- Da Cunha E., Charlot S., Elbaz D., 2008, *MNRAS*, 388, 1595
- De Lucia G., Blaizot J., 2007, *MNRAS*, 375, 2
- Díaz-García L. A., et al., 2015, *A&A*, 582, A14
- Doi M., et al., 2010, *AJ*, 139, 1628
- Dupke R. a., Benítez N., Moles M., Sodre L., J-PAS Collaboration 2015, IAU General Assembly, 29, #2257789
- Faber S. M., 1972, *A&A*, 20, 361
- Fagotto F., Bressan A., Bertelli G., Chiosi C., 1994a, *A&AS*, 104
- Fagotto F., Bressan A., Bertelli G., Chiosi C., 1994b, *A&AS*, 105
- Falcón-Barroso J., Sánchez-Blázquez P., Vazdekis A., Ricciardelli E., Cardiel N., Cenarro A. J., Gorgas J., Peletier R. F., 2011, *A&A*, 532, A95
- Gallazzi A., Charlot S., Brinchmann J., White S. D. M., Tremonti C. A., 2005, *MNRAS*, 362, 41
- Gallazzi A., Brinchmann J., Charlot S., White S. D. M., 2008, *MNRAS*, 383, 1439
- Giavalisco M., et al., 2004, *ApJ*, 600, L93
- Girardi L., Bressan A., Chiosi C., Bertelli G., Nasi E., 1996, *A&AS*, 117, 113
- González Delgado R. M., et al., 2014, *ApJ*, 791, L16
- Gonzalez J. J., Faber S. M., Worthey G., 1993, in *American Astronomical Society Meeting Abstracts*. p. 1355
- Greggio L., 1997, *MNRAS*, 285, 151
- Guo Q., et al., 2016, *MNRAS*, 461, 3457
- Hansson K. S. A., Lisker T., Grebel E. K., 2012, *MNRAS*, 427, 2376
- Hayward C. C., Smith D. J. B., 2015, *MNRAS*, 446, 1512
- Howell S. B., 2006, *Handbook of CCD Astronomy*. Cambridge University Press
- Kauffmann G., 1996, *MNRAS*, 281, 487
- Kauffmann G., et al., 2003, *MNRAS*, 341, 33
- Kobayashi M. A. R., Inoue Y., Inoue A. K., 2013, *ApJ*, 763, 3
- Koekemoer A. M., et al., 2011, *ApJ*, 197, 36
- Kriek M., Conroy C., 2013, *ApJ*, 775, L16
- Kriek M., van Dokkum P. G., Labbé I., Franx M., Illingworth G. D., Marchesini D., Quadri R. F., 2009, *ApJ*, 700, 221
- Kriek M., et al., 2010, *ApJ*, 722, L64
- Kroupa P., 2001, *MNRAS*, 322, 231
- Lanz T., Hubeny I., 2003a, *ApJS*, 146, 417
- Lanz T., Hubeny I., 2003b, *ApJS*, 147, 225
- Lanz T., Hubeny I., 2007, *ApJS*, 169, 83
- Lara-López M. A., et al., 2010, *A&A*, 521, L53
- Le Borgne J.-F., et al., 2003, *A&A*, 402, 433
- Lee S.-K., Idzi R., Ferguson H. C., Somerville R. S., Wiklind T., Giavalisco M., 2009, *ApJS*, 184, 100
- Lee S.-K., Ferguson H. C., Somerville R. S., Wiklind T., Giavalisco M., 2010, *ApJ*, 725, 1644
- Lee K.-S., et al., 2011, *ApJ*, 733, 99
- MacArthur L. A., González J. J., Courteau S., 2009, *MNRAS*, 395, 28
- MacArthur L. A., McDonald M., Courteau S., Jesús González J., 2010, *ApJ*, 718, 768

Madau P., Dickinson M., 2014, *ARA&A*, 52, 415
 Magris G., Mateu P. J., Mateu C., Bruzual A. G., Cabrera-Ziri I., Mejía-Narváez A., 2015, *PASP*, 127, 16
 Maraston C., 2005, *MNRAS*, 362, 799
 Maraston C., Greggio L., Renzini A., Ortolani S., Saglia R. P., Puzia T. H., Kissler-Patig M., 2003, *A&A*, 400, 823
 Maraston C., Pforr J., Renzini A., Daddi E., Dickinson M., Cimatti A., Tonini C., 2010, *MNRAS*, 407, 830
 Marin-Franch A., Taylor K., Cenarro J., Cristobal-Hornillos D., Moles M., 2015, IAU General Assembly, 29, 2257439
 Martins L. P., González Delgado R. M., Leitherer C., Cerviño M., Hauschildt P., 2005, *MNRAS*, 358, 49
 Mitchell P. D., Lacey C. G., Baugh C. M., Cole S., 2013, *MNRAS*, 435, 87
 Moles M., et al., 2008, *AJ*, 136, 1325
 Morgan W. W., 1956, *PASP*, 68, 509
 Naab T., Ostriker J. P., 2017, *ARA&A*, 55
 Ocvirk P., Pichon C., Lançon A., Thiébaud E., 2006, *MNRAS*, 365, 46
 Oyaizu H., Lima M., Cunha C. E., Lin H., Frieman J., Sheldon E. S., 2008, *ApJ*, 674, 768
 Pacifici C., Charlot S., Blaizot J., Brinchmann J., 2012, *MNRAS*, 421, 2002
 Panter B., Jimenez R., Heavens A. F., Charlot S., 2008, *MNRAS*, 391, 1117
 Pforr J., Maraston C., Tonini C., 2012, *MNRAS*, 422, 3285
 Pforr J., Maraston C., Tonini C., 2013, *MNRAS*, 435, 1389
 Prugniel P., Vauglin I., Koleva M., 2011, *A&A*, 531, A165
 Rauch T., 2003, *A&A*, 403, 709
 Renzini A., 2006, *ARA&A*, 44, 141
 Rodríguez-Merino L. H., Chavez M., Bertone E., Buzzoni A., 2005, *ApJ*, 626, 411
 Rosales-Ortega F. F., Sánchez S. F., Iglesias-Páramo J., Díaz A. I., Vílchez J. M., Bland-Hawthorn J., Husemann B., Mast D., 2012, *ApJ*, 756, L31
 Salim S., Lee J. C., Ly C., Brinchmann J., Davé R., Dickinson M., Salzer J. J., Charlot S., 2014, *ApJ*, 797, 126
 Salpeter E. E., 1955, *ApJ*, 121, 161
 Sánchez-Blázquez P., et al., 2006, *MNRAS*, 371, 703
 Sánchez S. F., et al., 2012, *A&A*, 538, A8
 Sánchez S. F., et al., 2013, *A&A*, 554, A58
 Smith D. J. B., Hayward C. C., 2015, *MNRAS*, 453, 1597
 Sorba R., Sawicki M., 2015, *MNRAS*, 452, 235
 Strateva I., et al., 2001, *AJ*, 122, 1861
 Taylor E. N., Franx M., Brinchmann J., van der Wel A., van Dokkum P. G., 2010, *ApJ*, 722, 1
 Tinsley B. M., 1972, *A&A*, 20, 383
 Tinsley B. M., 1980, *Fund. Cosmic Phys.*, 5, 287
 Tojeiro R., Heavens A. F., Jimenez R., Panter B., 2007, *MNRAS*, 381, 1252
 Tremonti C. A., et al., 2004, *ApJ*, 613, 898
 Vogelsberger M., et al., 2014, *MNRAS*, 444, 1518
 Walcher J., Groves B., Budavári T., Dale D., 2011, *Ap&SS*, 331, 1
 Westera P., Lejeune T., Buser R., Cuisinier F., Bruzual G., 2002, *A&A*, 381, 524
 White S. D. M., Frenk C. S., 1991, *ApJ*, 379, 52
 Wolf C., Meisenheimer K., Rix H.-W., Borch A., Dye S., Kleinheinrich M., 2003, *A&A*, 401, 73
 Wood D. B., 1966, *ApJ*, 145, 36
 Worthey G., 1994, *ApJS*, 95, 107
 Wuyts S., Franx M., Cox T. J., Hernquist L., Hopkins P. F., Robertson B. E., van Dokkum P. G., 2009, *ApJ*, 696, 348
 York D. G., et al., 2000, *AJ*, 120, 1579
 Zibetti S., Gallazzi A., Charlot S., Pierini D., Pasquali A., 2013, *MNRAS*, 428, 1479

APPENDIX A: BUILDING THE MOCK SAMPLE

A1 Mock galaxy parameters

The Synthetic Spectral Atlas of Galaxies (SSAG) built by [Cabrera-Ziri & Mejía-Narváez \(2014\)](#) is a collection of 10k Monte Carlo realisations of the recipe for the star formation rate $\Psi(t)$ introduced

by [Chen et al. \(2012, C12 hereafter\)](#). For details on the probability distribution function (PDF) and the physical motivation supporting the choice of the 11 parameters entering the C12 definition of $\Psi(t)$, see C12 and [Kauffmann et al. \(2003\)](#). In summary, the C12 SFR's have three main components, namely: an underlying exponentially declining rate, with initial onset at $t = t_{\text{form}}$, and e -folding time τ (a τ -model); a burst of constant star formation parametrised by a random amplitude $A \equiv M_{\text{burst}}/M_{\text{cont}}$, which blends with the τ -model at a random time t_{burst} between t_{form} and the present, and lasts for t_{ext} ; and a truncated regime, where $\Psi(t)$ starts declining faster than before at $t = t_{\text{trunc}}$, with e -folding time $\tau_{\text{trunc}} < \tau$. The stellar metallicity Z of the mock galaxy is selected from the range allowed by the BC03 models, $0.0001 \leq Z \leq 0.05$. Following C12, we use the two-phase starlight dust extinction model by [Charlot & Fall \(2000\)](#), defined by the optical depth τ_V in the V -band when the stellar population is still in the birth cloud ($t < 10^7$ yr), and the fraction μ of τ_V that characterises the interstellar medium after the birth cloud is dissipated ($t > 10^7$ yr). To account for stellar kinematics effects, the resulting SED is broadened using a Gaussian kernel with velocity dispersion σ_V . The PDF of the C12 SFH parameters is built assuming they are uncorrelated. We recognise this as a weakness of the C12 recipe, since, for instance, the random selection of the values of Z , σ_V , τ_V , μ , and t_{form} most likely will not reproduce the known correlations among these parameters. The values of the 11 C12 parameters, t_{form} , τ , t_{burst} , t_{ext} , A , t_{trunc} , τ_{trunc} , Z , σ_V , τ_V , and μ defining the SFH for a fraction of the galaxies in our mock sample are listed in Table A1, columns (1) to (11).

Once $\Psi(t)$ has been specified, the SED $F_\lambda(t)$ of the composite population in the mock galaxy is computed as in ([Bruzual & Charlot 2003, BC03 hereafter](#))¹¹,

$$F_\lambda(t) = \int_0^t \Psi(t-t') f_\lambda(t', Z) dt', \quad (\text{A1})$$

where $f_\lambda(t, Z)$ is the SED at age t of a simple stellar population (SSP) for the chosen initial mass function (IMF) and metallicity Z . For $f_\lambda(t, Z)$ we use the XMLESS version (BC03xm hereafter) of the BC03 models, described below. We note that the implementation of the SSAG by [Cabrera-Ziri & Mejía-Narváez \(2014\)](#) used by M15 is based on the standard BC03 models. The following properties of each mock galaxy, $\log M_*/M_\odot$ (log stellar mass), $\langle \log t_*/\text{yr} \rangle_M$ (mass-weighted mean log age), $\langle \log t_*/\text{yr} \rangle_L$ (luminosity-weighted mean log age), and A_V (extinction in the V -band) are listed in columns (12) to (15) of Table A1, in order of increasing present-day $u-r$ colour (column 16). The values of $\log M_*/M_\odot$, $\langle \log t_*/\text{yr} \rangle_M$, $\langle \log t_*/\text{yr} \rangle_L$, Z , and A_V in Table A1 are the *true values* used to compute the residuals of these properties in this paper (Eq. 11). We note that $\log M_*/M_\odot$, $\langle \log t_*/\text{yr} \rangle_M$, and Z are independent of the SSP models in use, whereas $\langle \log t_*/\text{yr} \rangle_L$, A_V , and $u-r$ do depend on these models¹².

A2 The BC03 XMLESS models

We have built new evolutionary population synthesis models based on the BC03 *Padova 1994* set of stellar evolutionary tracks ([Alongi et al. 1993; Bressan et al. 1993; Fagotto et al. 1994a,b; Girardi et al.](#)

¹¹ The software to perform this convolution for the C12 $\Psi(t)$ is available at <http://www.bruzual.org/src.tgz>

¹² The complete version of Table A1 and the full set of SEDs for the mock galaxy sample can be downloaded in digital form from http://www.bruzual.org/mn_et_al_2017/

Table A1. Star formation history and stellar population parameters of a fraction of the mock galaxy sample.

(1)	(2)	(3)	(4)	(5)	(6)	(7)	(8)	(9)	(10)	(11)	(12)	(13)	(14)	(15)	(16)
t_{form} (Gyr)	$1/\tau$ (Gyr $^{-1}$)	t_{burst} (Gyr)	t_{ext} (Myr)	A	t_{trunc} (Gyr)	τ_{trunc} (Myr)	Z (Z_{\odot})	σ_v (km s $^{-1}$)	τ_V	μ	$\log M_*$ (M_{\odot})	$\langle \log t_* \rangle_M$ (yr)	$\langle \log t_* \rangle_L$ (yr)	A_V (mag)	$u-r$ (ABmag)
1.90	0.033	1.04	202.56	0.32	1.78	141.11	0.540	0.176	-1.100	8.458	8.880	0.145	0.971
1.61	0.657	1.14	286.12	0.18	0.81	233.31	1.33	392.79	0.743	0.324	-0.063	9.331	9.846	0.616	1.721
6.00	0.651	4.81	255.00	0.04	1.55	371.21	0.217	0.406	0.147	9.178	9.424	0.294	1.879
2.50	0.090	2.18	202.56	0.66	1.28	314.41	0.27	251.19	1.247	0.432	0.581	8.908	9.167	0.708	1.905
4.50	0.581	2.63	255.00	0.98	1.40	101.57	2.443	0.115	0.222	9.269	9.405	0.016	1.970
2.60	0.234	2.60	64.05	0.14	0.81	232.86	1.35	142.10	1.193	0.469	0.008	9.412	9.633	0.098	1.979
6.00	0.522	2.58	202.56	1.62	2.00	287.74	2.08	141.42	0.633	0.313	0.027	9.888	9.918	0.352	2.434
9.50	0.616	4.06	127.80	1.37	1.35	287.55	0.568	0.342	0.300	9.510	9.586	0.157	2.455
8.25	0.378	7.73	101.52	0.14	1.02	715.37	1.37	54.11	1.989	0.492	0.034	9.568	9.762	1.068	2.580
12.25	0.990	4.00	255.00	0.17	2.32	78.53	3.090	0.666	0.068	10.016	10.034	0.852	3.414

Table A2. Spectral properties of different stellar atlases relevant in the UV, as published.

Stellar Library	Stellar Type	Wavelength Range	$R_{\text{STEP}} = \frac{\lambda}{\Delta\lambda}$	Reference
Tlusty	O stars	45 Å — 300 μm	26,000 — 38,000	Lanz & Hubeny (2003a,b)
Tlusty	B stars	54 Å — 300 μm	100,000 — 200,000	Lanz & Hubeny (2007)
Martins et al.	A stars	3000 — 7000 Å	10,000 — 23,000	Martins et al. (2005)
UVBlue	F,G,K stars	850 — 4700 Å	50,000	Rodríguez-Merino et al. (2005)
Rauch	T>55MK	5 — 2000 Å	50 — 20,000	Rauch (2003)

1996), but using updated libraries of theoretical and empirical stellar spectra. Table A2 lists the spectral characteristics of the model spectra relevant in the UV range for stars of different T_{eff} , as published. In the 4th column of this table, we indicate R as R_{STEP} to emphasise that in this case we use the *wavelength step* $\Delta\lambda$ to measure R , as defined in Coelho (2014). To express the UV spectra in a common wavelength scale, we downgrade in resolution the spectra listed in the first two rows of Table A3 using a Gaussian smoothing function centred at each wavelength point λ_i , sampled according to the step in the 2nd column of Table A3,

$$f(\lambda) = \frac{1}{\sigma_{\lambda}\sqrt{2\pi}} \exp\left[-\frac{(\lambda - \lambda_i)^2}{2\sigma_{\lambda}^2}\right], \quad (\text{A2})$$

where,

$$\sigma_{\lambda} = \frac{\Delta\lambda}{2\sqrt{2}\log 2} = 0.4247\Delta\lambda. \quad (\text{A3})$$

In this case $\Delta\lambda$ is the FWHM listed in the 3rd column of Table A3. We resample the smoothed spectra with a uniform step = 0.9 Å for λ in the range 5.6 — 911 Å, and = 0.5 Å for λ in the range 911 — 3540.5 Å, as indicated in Table A3. The spectral resolution in the UV range is then $R = \lambda/\Delta\lambda = \lambda/2.5$. The stellar spectra listed in the last three rows of Table A3 are used as distributed, with their original sampling and with no smoothing. The set of spectra described in Table A3 has been named XMILESS, to indicate the use of an extended version of the Miles+Stelib empirical libraries. Spectra of the corresponding $[Z/Z_{\odot}]$ from all the sources listed in Table A3 enter in the construction of the new BC03 models, de-

noted BC03xm hereafter. In this paper we use the BC03xm models computed for the Chabrier (2003) initial mass function (IMF).¹³

APPENDIX B: A CLOSER VIEW ON THE TTA

In §4 we explored the residuals behaviour by treating each SED in the mock sample, which was built upon 134 SFHs and $N_r = 20$ noise realisations, as a different galaxy. While several correlations arised resembling what is expected from the presence of the several degeneracies, it remains to be seen if such correlations are a consequence of the physical properties of the sample as a whole, i. e., different SFHs are located at different regions in the space of residuals, or if these correlations are intrinsic to the physical properties of the individual SFHs, i. e., the noise realisations of the same SFH scatter across the space of residuals according to the observed correlations; under the supposition that 20 noise realisations yield a representative sample around the maximum likelihood. In Fig. 6 we already showed that the strength of the several degeneracies is independent of the presence of noise in the data, a result that hints towards an intrinsic origin.

We emphasise that these distributions are not related to the posterior PDF in a Bayesian sense, in which case those would carry information on the whole parameter space, restricted only by the prior PDF. In this case, by SED-fitting the N_r noise realisations we are just sampling the likelihood around the $\hat{\mathbf{x}}$ of each mock SFH, which statistical dispersion will tell us (at most) how flat or sharp the *absolute maximum* of the corresponding likelihood is. The best and worst fitting solutions among the N_r will have in general very

¹³ The BC03 and BC03xm models for the Salpeter (1955), Kroupa (2001), and Chabrier (2003) IMFs are available at http://www.bruzual.org/bc03/Updated_version_2016/

Table A3. Wavelength coverage versus spectral atlas adopted in the BC03 XMLESS models.

Wavelength Range (Å)	Sampling Step (Å)	FWHM $\Delta\lambda$ (Å)	Stellar Library	Reference
5.6—911	0.9	2.0	Tlusty, Martins et al., UVBlue, Rauch	Table A2
911—3540.5	0.5	1.0	Tlusty, Martins et al., UVBlue, Rauch	Table A2
3540.5—7351	0.9	2.5	Miles	Sánchez-Blázquez et al. (2006); Falcón-Barroso et al. (2011); Prugniel et al. (2011)
7351—8750	1.0	3.0	Stelib	Le Borgne et al. (2003)
8750—36000	variable	variable	BaSeL 3.1	Westera et al. (2002); Treatment of TP-AGB stars as in BC03

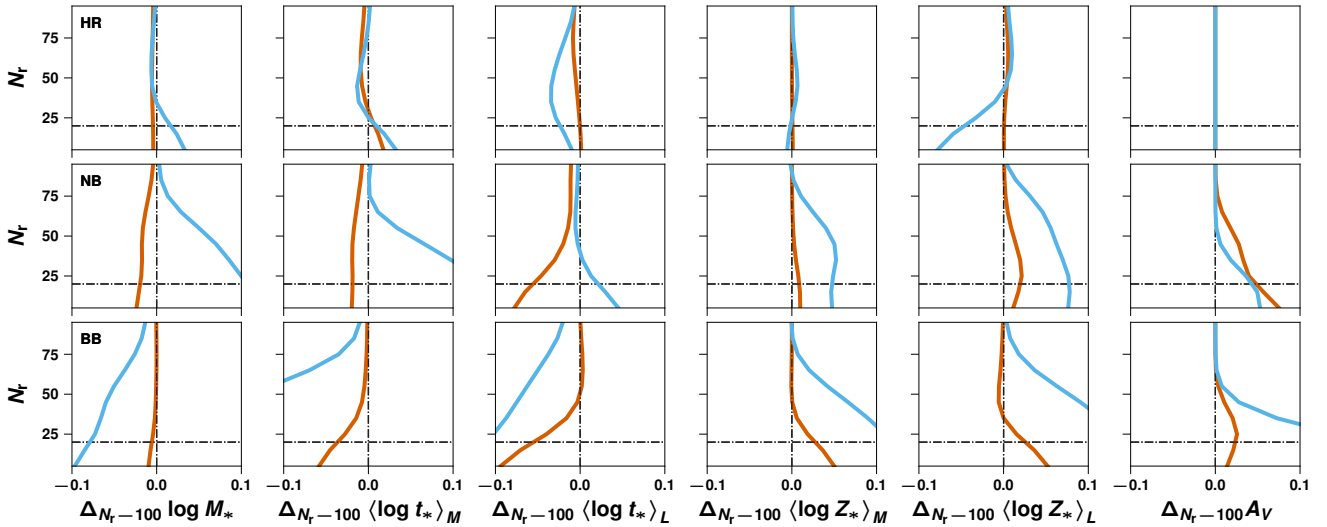


Figure B1. The bias difference between a 100-realizations and a N_r -realizations experiment (labelled $\Delta_{N_r-100,x}$) for a SFG (blue) and a PaG (orange) is shown for the studied physical properties retrieved from fitting SEDs at the HR, NB and BB spectral resolutions. The bias for the PaG converge quickly towards the 100-realizations bias, however in the case of BB results it is clear that $N_r > 20$ noise realisations are needed to reach statistical stability. For the SFG the results are even worse in most cases at all spectral resolutions. Interestingly, the convergence of dust extinction residuals at the HR resolution is very fast regardless of the galaxy type, a result consistent with a robust estimation (cf. Fig. 5). In summary, a conservative figure for the number of realisations would be 80 to reach statistical stability at all spectral resolutions shown. See text for details.

similar $\chi^2(\hat{\mathbf{x}})$ values, whereas the properties $\hat{\mathbf{x}}$ may indeed be considerably different (cf. Fig. B2). This fact is the main reason why we assess our results in terms of the recovered physical properties and not in terms of the goodness-of-fit.

B1 On the number of noise realisations

To test the effects of the assumed $N_r = 20$ noise realisations, we select two galaxies representative of the SFGs and the PaGs. We compute for each spectral resolution (HR, NB and BB) $N_r = 100$ noise realisations and apply our SED-fitting procedure (as for the mock sample) to the 600 spectra. For the resulting physical properties we compute the bias as defined in §3.3 using the 100 realisations, and then compare this bias to the one obtained from several values of N_r in the range 5—95. We note that $N_r = 100$ is also an arbitrary choice and as such it may not yield statistical stability to the residual distributions. Nonetheless, this experiment may allow us to develop some insight into the pace of convergence of the statistical results. In Fig. B1 we show the bias difference, $\Delta_{N_r-100,x}$, for all the physical properties of interest in this paper, at all spectral resolutions, as a function of the N_r . It is clear that $N_r = 20$ is not enough in most cases, particularly at the NB and BB resolutions for

the PaG. For the SFG, the results are even worse, specially at the BB resolution. We conclude that, in order to study the mock sample on a SFH per SFH basis, at least $N_r = 80$ to reach statistical stability at the HR, NB and BB spectral resolutions. Since in §4 we explored the residual distribution statistics on a SED by SED basis, the assumed $N_r = 20$ probably has a negligible impact.

B2 On the residuals of individual SFHs

Fig. B2 shows the residual distributions of four SFGs (top rows) and four PaGs (bottom rows) over their corresponding 20 noise realisations. The median residual is represented by the arrows at the HR, NB and BB spectral resolutions (light blue, dark blue and grey, respectively). The HR determinations are, in general, less biased and more precise, as signaled by the dispersion of the distributions, with a tendency to slightly improve towards PaGs. The NB and BB, on the other hand, show larger biases and imprecisions in SFGs, with a remarkable improvement towards PaGs. From the histograms in Fig. B2 we compute the median and the 16 and 84th percentiles. In Fig. B3 we represent these median values in 134 dots, along with the 16—84th percentile range (cross), at the three spectral resolutions HR, NB and BB. The observed behaviour resembles

the one in Fig. 5 to great extent, which then again demonstrates the intrinsic origin of these correlations.

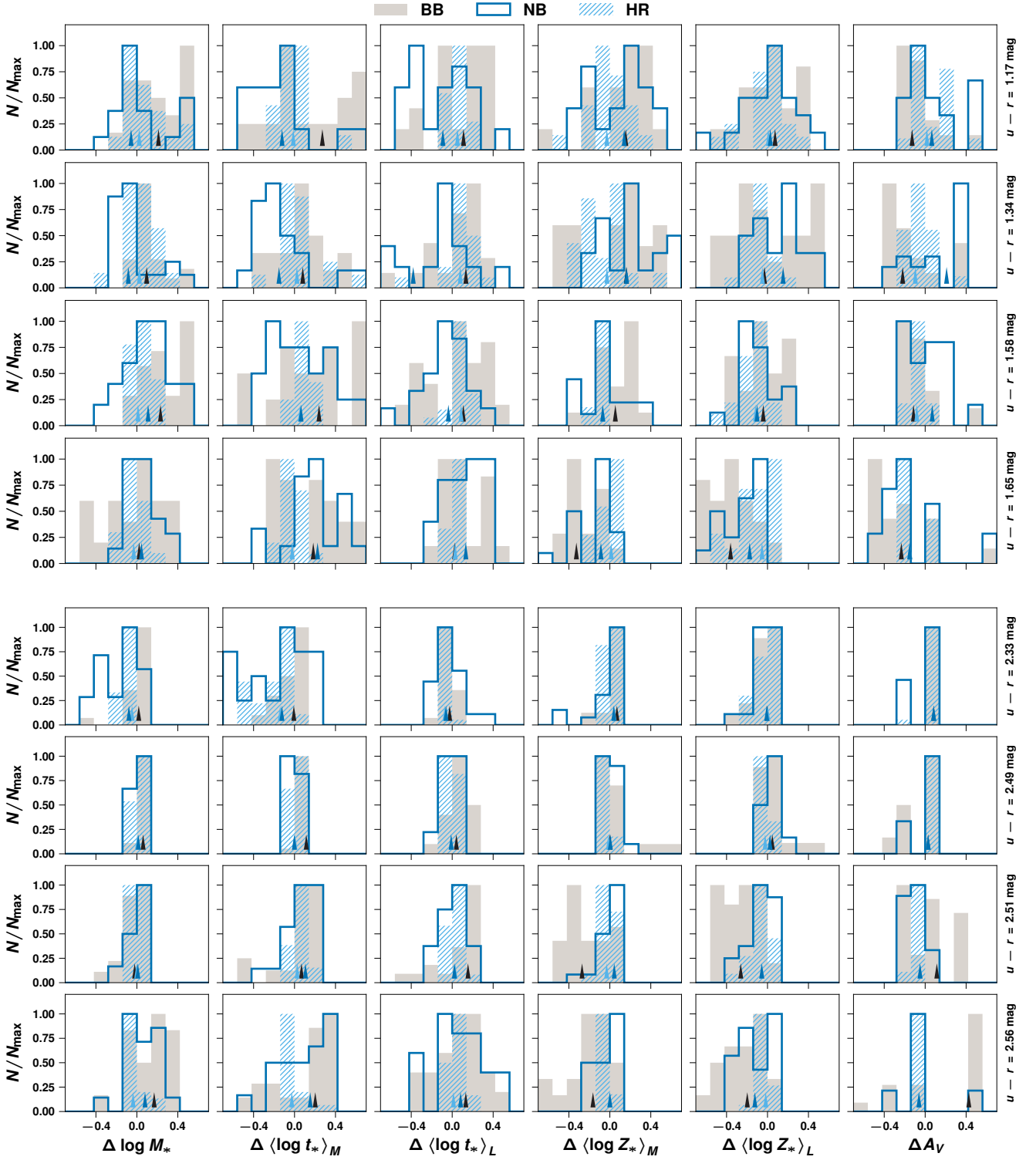


Figure B2. *Top four rows:* The residual distributions over the 20 noise realisations for four SFGs in the several physical properties we study in this paper. *Bottom four rows:* Same as top frame, but for PaGs. HR spectroscopy shows high residuals with low statistical dispersion in all physical properties, with a mild increment of the precision towards PaGs, whereas lower resolution NB and BB residuals are usually disperse in the observed range, with a remarkable increment in the precision towards PaGs. See text for details. The median residuals at the three spectral resolutions represented by the arrows in each plane are usually low in HR determinations, whereas NB and BB exhibit larger biases for SFGs, and biases comparable to HR for PaGs.

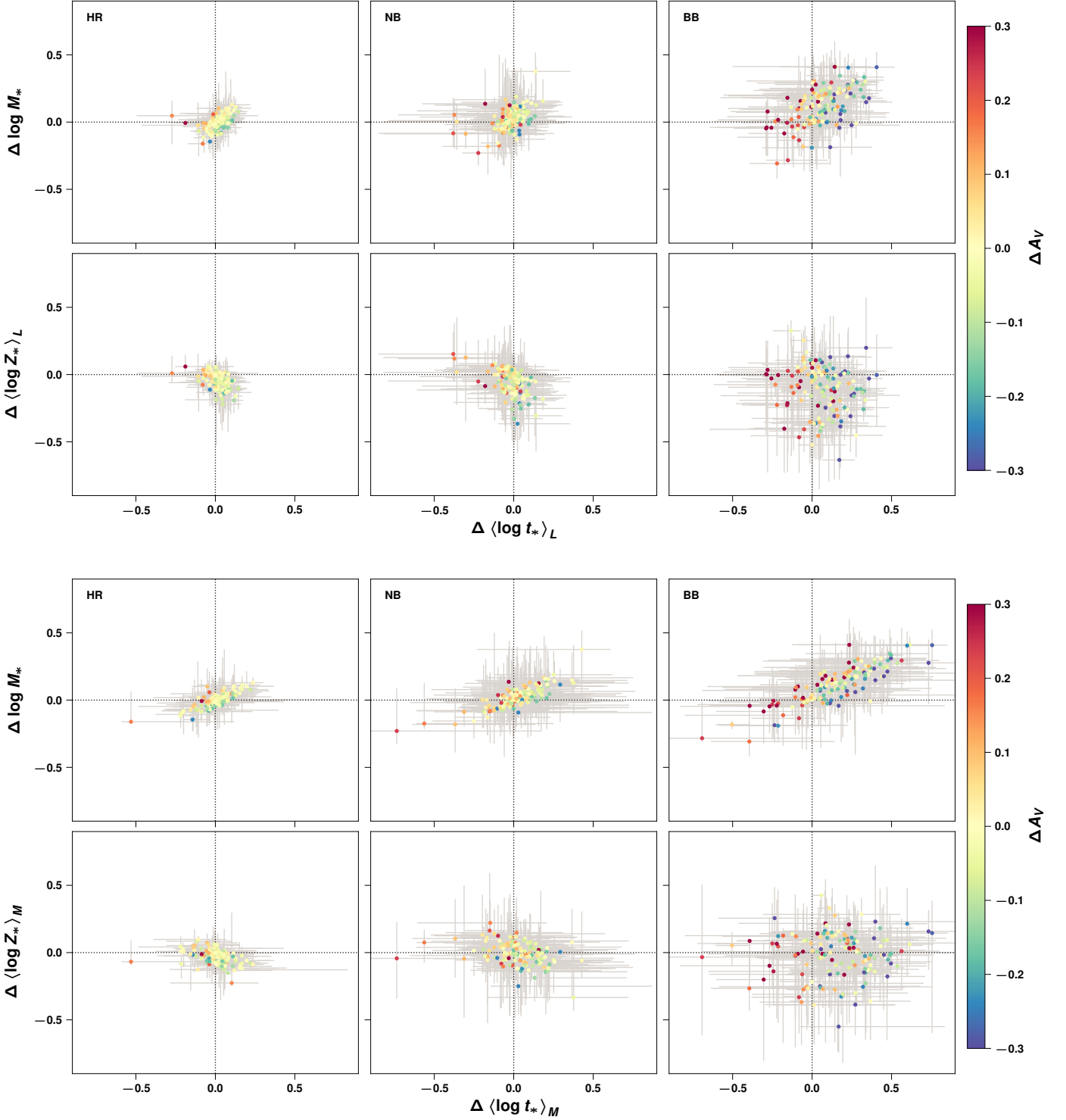


Figure B3. *Top:* The residuals for the several physical properties we discuss in this paper. Each point and cross represents the median and the 16—84th percentile range of the residuals for each galaxy in the mock sample over the 20 noise realisations. It is clear that the trends (whenever present) remain the same as in Fig. 5. *Bottom:* Same as top frame, but for the mass-weighted mean age and metallicity. See text for details.